Contrasted Summer Processes in the Sea Ice for Two Neighboring Floes North of 84°N: Surface and Basal Melt and False Bottom Formation

Christine Provost, Nathalie Sennéchael, Jérôme Sirven

JGR Oceans

RESEARCH ARTICLE
10.1029/2019JC015000

Contrasted Summer Processes in the Sea Ice for Two Neighboring Floes North of 84°N: Surface and Basal Melt and False Bottom Formation

Christine Provost[1], **Nathalie Sennéchael**[1], **and Jérôme Sirven**[1]

[1]Laboratoire LOCEAN-IPSL, Sorbonne Université (UPMC, Univ. Paris 6), CNRS, IRD, MNHN, Paris, France

Key Points:
- We present continuous observations in the high Arctic over the full summer season at two nearby sites with distinct initial conditions
- One site experienced a deep melt pond, sudden pond drainage, "false bottom" formation, and migration; the other site experienced continuous basal melt
- We report surface, internal, and basal processes in summer leading to drastic transient or more persistent ice structure transformations

Correspondence to:
C. Provost,
cp@locean-ipsl.upmc.fr

Citation:
Provost, C., Sennéchael, N., & Sirven, J. (2019). Contrasted summer processes in the sea ice for two neighboring floes north of 84°N: Surface and basal melt and false bottom formation. *Journal of Geophysical Research: Oceans*, *124*. https://doi.org/10.1029/2019JC015000

Received 25 JAN 2019
Accepted 19 MAY 2019
Accepted article online 27 MAY 2019

Abstract We report continuous observations in the high Arctic (north of 84°N) over the full 2013 summer season at two nearby sites with distinct initial snow depth, ice thickness, and altitude with respect to the local ice topography. The two sites, subject to similar atmospheric conditions that did not favor strong ice melt, showed contrasting evolutions. One site, with initially thin sea ice (1.40 m) at a relatively low location of the floe, witnessed the formation of a spectacular 1.20-m-deep melt pond, a pond-enhanced erosion of the ice surface, and a sudden pond drainage into the ocean. Then, the outpoured fresh water rapidly froze, heated the old ice from below, and also acted as a temporary shield from the ocean heat flux while it was progressively ablated through dissolution. Eventually, the site almost recovered its initial ice thickness. In contrast, the other site, with initially thicker sea ice (1.75 m) at a relatively high location on its floe, did not support any significant meltwater and underwent over 0.5 m of continuous basal ablation. The two sites experienced formation of superimposed and interposed ice. Sea ice survived summer melt at the two sites, which entered the refreezing season with similar snow and ice thicknesses. For the first time, processes associated with the formation of a deep melt pond and subsequent false bottom evolution are continuously documented with ice mass balance instruments.

Plain Language Summary Summer processes in the sea ice in a changing Arctic are documented at two nearby sites in the high Arctic (north of 84°N) in summer 2013. We report the first continuous observations of the formation of a melt pond more than 1.2 m deep, and the evolution of the fresh water after it outpoured to the ocean through a drainage hole at one site located in a topographic low. A nearby site, located on a topographic high, experienced very different evolution with no meltwater retention at the surface and continuous basal melting.

1. Introduction

During summer, the Arctic sea ice undergoes dramatic changes. The snow cover melts, exposing sea ice to solar radiation, and then the sea ice melts at its upper surface. Some of the meltwater drains vertically through the sea ice, contributing to desalination through brine flushing (e.g., Notz & Worster, 2009), while some is retained on the surface where it forms melt ponds with depths ranging from several centimeters to more than a meter (Eicken, 1994). The surface albedo lowers wherever melt ponds form (Perovich et al., 2002), and enhanced absorption of sunlight in the ice and the upper ocean accelerates ice melt (Eicken, 1994; Perovich et al., 2003).

Different factors affect melt ponding: snow cover as the initial source of meltwater, ice surface topography, which controls lateral meltwater transport and locations where water accumulates, and sea ice porosity and the drainage holes that govern meltwater vertical transport through the ice, eventually to the ocean (e.g., Eicken et al., 2002). Melt ponds are observed above sea level upon permeable warm ice, when intruding fresh meltwater freezes within the porous matrix of sea ice and forms interposed fresh ice plugs capable of retaining meltwater above hydraulic equilibrium (Eicken et al., 2004; Polashenski et al., 2012, 2017). The meltwater flux can also proceed through thaw holes, reach sea water beneath the ice, accumulate in bottom depressions, and form fresh water lenses or under-ice melt ponds (e.g. Eicken et al., 2002). As fresh water comes into contact with sea water, a supercooled transition layer occurs and underwater ice called a "false bottom" is formed (e.g., Eicken et al., 2002; Polashenski et al., 2012). The underwater fresh ice then progressively disappears due to bottom ablation. These summer processes are difficult to measure nondestructively.

We report continuous observations in the high Eurasian Arctic (north of 84°N) over the summer season from early April to late September 2013 at two nearby sites (A and B, always within 18-km distance) with different initial snow depth, ice thickness, and position with respect to the local ice floe topography. Though the two sites were subject to similar atmospheric conditions, they underwent contrasting evolution in snow depth, ice temperature and thickness, meltwater retention, and meltwater fate. Site A witnessed the formation of a spectacular 1.20-m-deep melt pond, sudden meltwater outpouring into the ocean, and subsequent false bottom formation. In contrast, sea ice at site B did not support any significant melt pond and underwent drastic alteration with over 0.5 m of basal melt. In both cases, sea ice survived summer melt, and, at the beginning of the freezing period, the two sites had similar ice thicknesses. Sea ice at site A had almost recovered its initial ice thickness.

In this paper we focus on the numerous processes that transform Arctic sea ice in summer as they are continuously documented at the two sites. These include snowmelt, meltwater fate, superimposed ice, melt pond, interposed ice, pond-enhanced surface erosion, false bottom growth and erosion, and basal ablation. The paper is organized as follows. Section 4 presents the experimental setup, the environmental conditions, the data, and their processing. The evolution of snow and ice along the drift at the two sites is then described in section 3, broken down into the premelt period (section 3.1), the melt period (section 3.2), and the refreezing period (section 3.3). The melt period section, the largest section, comprises four subsections, snowmelt, melt pond, meltwater pathways including interposed ice, and false bottom. Section 4 discusses sea ice budgets at the two sites, desalination, and ice topography. Finally, section 5 summarizes the results and puts the work into perspective.

2. Data and Methods

2.1. Experimental Setup

The two sites, A and B, initially 12 km apart, drifted together from the North Pole toward Fram Strait with the Transpolar Drift. Site A featured an Ice Atmosphere Ocean Observing System (IAOOS) platform (Figure 1a) and a webcam 3 m away facing the buoy (Figure 1b). The IAOOS platform carried an ice mass balance instrument monitoring temperature across the air/snow/sea ice/ocean interfaces, an ocean profiler (data not used here) and a weather mast recording air temperature and atmospheric pressure. Site B only comprised an ice mass balance instrument secured on a buoy (Figure 1c).

The ice mass balance instrument was developed by the Scottish Association of Marine Science (Jackson et al., 2013). The Scottish Association of Marine Science sea ice mass balance for the Arctic (SIMBA) package comprises a 5-m-long chain cable hanging through air, snow, sea ice, and ocean (see setup in Figure 1). The chain comprises solid-state sensors located every 2 cm measuring temperature at approximately 0.1 °C accuracy (resolution 1/16 °C). Temperature was measured every 4 hr at site A (6 hr at site B; Table 1). The SIMBA features a heating mode which can discriminate between different media, especially between snow and ice (Jackson et al., 2013). The heating mode produces a short heat pulse (120 s); the temperature response to the short heat pulse depends on the heat conductivity and diffusivity of the medium (air, snow, ice, and water). Here, we use the temperature change after 120 s, ΔT_{120s}, which brings useful additional qualitative information on the thermal diffusivity of the different media. The heating mode was activated once a day.

The webcam was built and installed by the Polar Center from the Applied Physics Laboratory of the University of Washington (USA) for the IAOOS project and was surrounded with 10-cm-wide ablation stakes. The camera stood about 1.8 m above the ice surface in April. The camera provided four sets of images a day (burst mode can give up to four images every 6 hr) and valuable visual information about the weather and surface conditions (rain snow, wind, melt pond, ridges, and leads).

The two sites were instrumented from the Russia-operated ice camp Barneo on 17 April 2013 at 89.2°N and 65.4°W for site A and on 15 April at 89.3°N and 57.1°W for site B, 12 km away. The typical floe size was 500–1,500 m in diameter. The chain cable was deployed from a pole 2 m away from the buoy and through a 2-in. hole drilled through the ice. The two sites had different initial ice and snow conditions: site A featured a thick snow layer (0.52 m), a thin ice layer (1.42 m), and a small freeboard (0.05 m), while at site B the snow cover was thin (0.22 m), ice was thick (1.72 m), and the freeboard larger (0.17 m). The buoys drifted southward from April to July and remained meandering around 84°N and 0 meridian for 31 days (11 August to 11

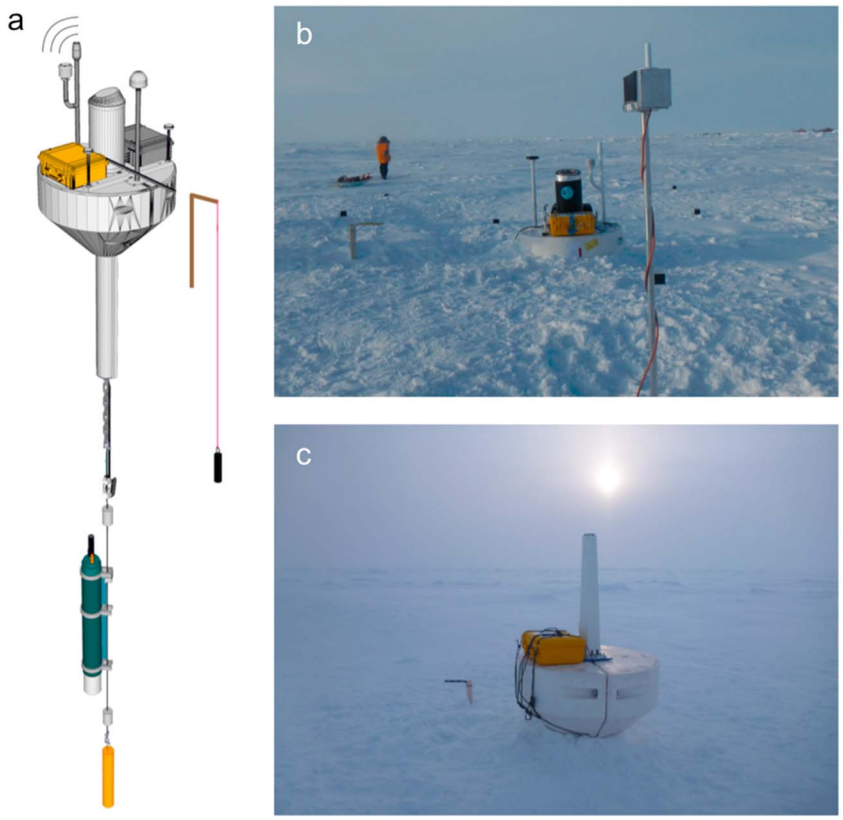

Figure 1. Experimental setup: (a) Schematics of IAOOS "Ice ocean atmosphere observing system" platform. (b) Experimental setup at site A (picture from deployment): the webcam (from NPEO, APL, USA) in the foreground is facing the IAOOS platform at a distance of 3 m, the SIMBA pelicase (containing GPS, antenna, central unit, and batteries) is secured on the IAOOS buoy, and the SIMBA chain is hanging from a wooden pole 2 m away from the buoy (to the left on the picture). Ablation stakes (10 cm wide, 1.80 long, 10-cm black and white stripes) are installed around the platform. (c) Experimental setup at site B (picture from deployment): the SIMBA central unit is attached on a buoy, and the SIMBA chain is hanging from a wooden pole (to the left).

September; Figure 2a). The buoys were recovered on 21 September by the Norwegian ice breaker KV Svalbard at 83.75°N and 4.42°W for site A (83.72°N and 4.05°W for site B), about 700 km from their deployment position after a 1,500-km-long meandering drift. At the time of recovery, each buoy was in the middle of a large ice floe with around 0.10 m of snow on 1.40- to 1.50-m-thick sea ice. Table 1 summarizes the measurement setup of the SIMBAs, the time intervals of the deployments, the initial and final snow, and ice thicknesses.

Table 1
Sampling Intervals, Initial, and Final Conditions at Sites A and B

Measurement setup	Site A	Site B
Sampling intervals (hr)		
GPS	2	2
Temperature	4	6
Heating cycle	24	24
Drift time		
Start	17 April	15 April
End	21 September	21 September
Record length (days)	157	159
Initial (final) thickness (m)		
Snow	0.52 (0.10)	0.22 (0.12)
Ice	1.42 (1.38)	1.72 (1.52)
Freeboard measured	0.05 (N/A)	0.17 (N/A)

2.2. Environmental Conditions From the Webcam, the Weather Mast, and ERA-Interim

We used surface information at site A from the webcam, the weather mast, and ERA-Interim (ERA-I) outputs (Dee et al., 2011) interpolated in time and space to the platform location (the two platforms are always within the same ERA-I grid cell). ERA-I outputs were compared to variables measured by the platform: sea level pressure (good agreement, not shown) and air temperature (Figure 2b). We observed the already documented (e.g., Simmons & Poli, 2015) warm air temperature bias present in ERA-I in the Arctic (here a +1.4 °C bias and 1.2 °C root-mean-square difference). Storms, which we define as ERA-I wind velocities exceeding 8 m/s during at least 1 day, were numerous (Figures 2c and 2d). Storms starting with southerly winds transported warm and moist air into the Central Arctic from the Atlantic Ocean (Figures 2b and 2d). The warm

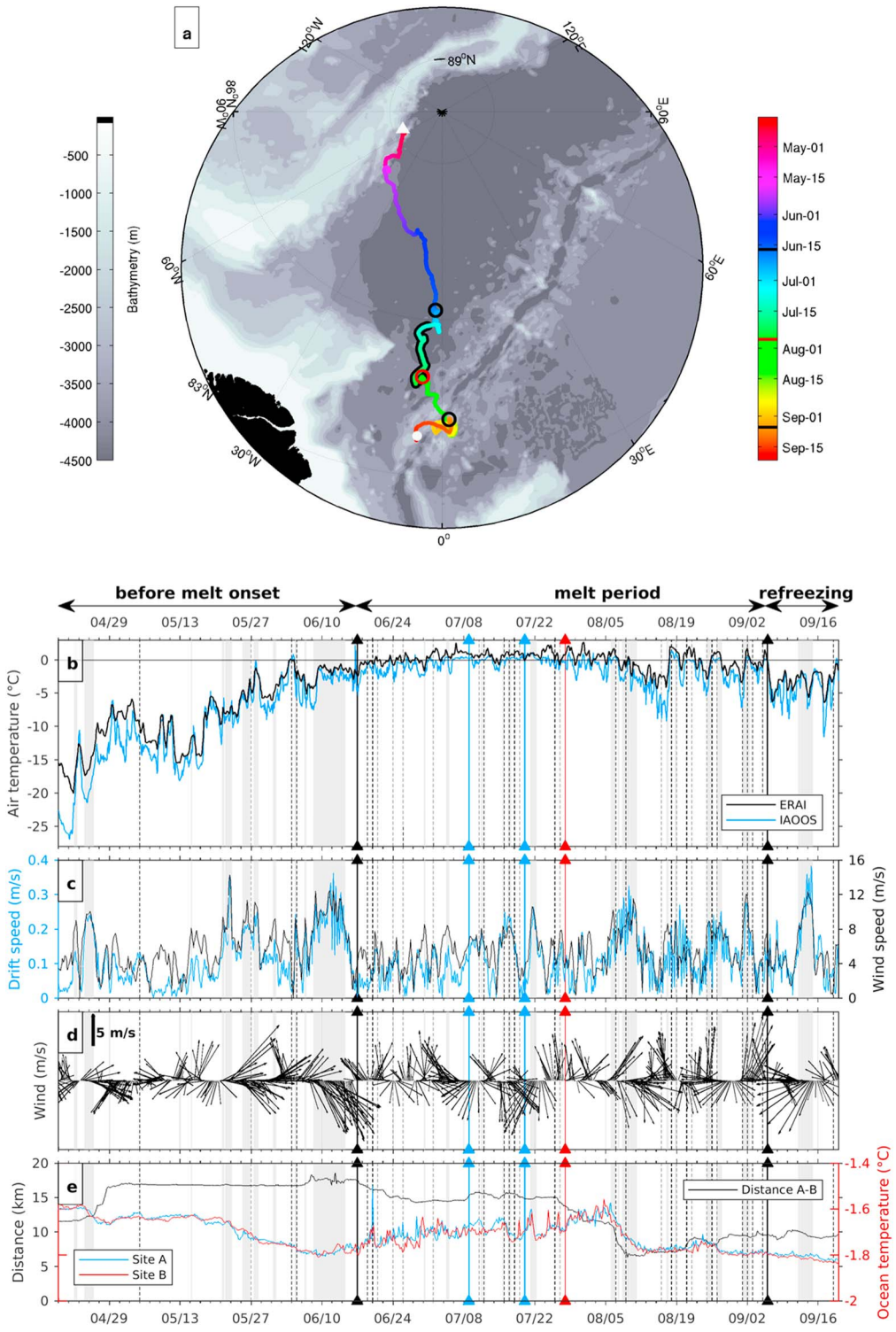

Figure 2. Drift trajectory and environmental parameters along the drift: (a) Trajectories of the site A buoy colored as a function of time. Background is bottom topography (m). (b) Air surface temperature (°C) from site A buoy surface unit (blue) and ERA-I (black) along the drift (*x* axis is time with ticks every 2 days). Time resolution is 1 hr for the buoy and 6 hr for ERA-I. (c) Buoy drift velocities (blue) and surface wind intensity from ERA-I (in black) in meters per second. (d) Surface wind vectors from ERA-I. (e) Distance (km) between site A and site B (in black), near-ice ocean temperature (°C; averaged temperature over the last meter of the sea ice mass balance for the Arctic chains; site A in blue and site B in red). Periods with wind velocities in excess of 8 m/s are shaded in gray; rain and snow events as seen in the webcam are indicated in vertical dashed lines. Melt onset and freeze onset are indicated in bold black. Times at which first puddles are seen in the background and at which melt pond water is seen reaching the base of the sea ice mass balance for the Arctic chain are indicated in blue. Date of meltwater drainage is in red.

air, rain, and snow deposition associated with these storms have an imprint in the SIMBA data as shown in the following sections. Sites A and B experienced similar drifts with hourly mean drift velocities that exceeded 0.2 m/s and peaked over 0.25 m/s during the storms (Figure 2c). The storms and southerly winds slowed down the southward drift and led to a meandering trajectory (Figure 2a). The distance between the two instruments varied from 6.4 to 18.6 km (mean value 13.5 km and standard deviation 3.5 km; Figure 2e).

Near-ice ocean temperatures at both sites decreased from about −1.6 °C on 21 April to a minimum of −1.8 °C around 10 June (Figure 2e): they were close to freezing temperatures and the decrease mostly reflected the well-known salinity change between fresher near-surface waters from the Canadian Basin to saltier near-surface waters in the Eurasian Basin (e.g., Athanase et al., 2019). Both sites then experienced increasing trends of near-ice ocean temperatures, from −1.8 °C on 10 June to less than −1.6 °C on 5 August with superimposed high-frequency fluctuations of small amplitude (Figure 2e). The temperature increase in the upper ocean close to the ice base was due to summer solar radiation, while large drift speeds induce mixing with deeper colder waters reducing temperature. The early (7 to 9) August storm was particularly efficient, inducing a temperature drop of 0.2 °C. After 9 August, near-ice ocean temperatures remained below −1.75 °C.

According to the Sun and time, the webcam was facing south most of the time suggesting little rotation of the floe. The webcam documented the rising of an ice ridge to the West (right) on 1 May, a lead opening to the South East on 14 June, snow accumulation and melt, and the development, rise, and drainage of a melt pond (Figure 3). Distances are not easy to estimate with the wide-angle lens of the camera. At recovery, the icebreaker KV Svalbard was in the lead opening and the distance to the buoy was about 200 m (Figure 3h). The webcam also provided information on atmospheric conditions in particular, rain, snow deposition, and strong wind episodes. Those events are reported in Figure 2.

2.3. Interfaces From the SIMBA Instruments

To define the interfaces between air, snow, ice, and ocean, we had to modify the procedure based on identifying changes in profiles of vertical and temporal derivatives of temperature as described for winter conditions by Provost et al. (2017). Summer quasi-isothermal conditions make interface detection more difficult than in winter. Furthermore, fresh meltwater percolating through snow and ice (leading to superimposed ice, interposed ice, and false bottoms) increases the number of interfaces that are not simply air-snow, snow-ice, and ice-ocean as in winter. As snow melts out, the main interfaces are called the lower boundary of the atmosphere, (which can be air-snow, air-pond water, or air-ice), upper boundary of sea ice (which can be snow-ice, superimposed ice-ice, or meltwater-ice), and upper ocean boundary (which can be sea ice-ocean or false bottom ocean). The temperature, its vertical and temporal derivatives, and the heated temperature after 120 s (ΔT_{120s}) are shown in Figures 4 and 5 with the main interfaces. Figure 6 shows three examples of typical temperature profiles at sites A and B with the interfaces.

To estimate the position of the *lower boundary of the atmosphere*, we started from the top of the chain and looked for a sharp increase in the vertical gradient and a simultaneous decrease in the temperature standard deviation over periods of 24, 48, and 72 hr. This semiautomatic procedure provides a satisfying interface consistent with the time derivative of temperature and the heated temperature (Figures 4 and 5). Both sites experienced snow thickness increase until mid-June and snowmelt until mid-July. Site A sustained a melt pond in late July while site B did not, and both sites showed a thin and variable layer of snow afterward. The lower boundary of the atmosphere cannot be determined for several days as the SIMBA chain is either totally in the snow (site B in mid-June) or below the melt pond surface (site A on 25 and 26 July; Figures 4 and 5).

The position of the *upper boundary of sea ice* is initially derived from the sharp contrast in ΔT_{120s} between both media. This is easy to identify at both sites until 17 June while the snow/ice interface does not change (Figure 6). After 17 June, the determination of interfaces requires a careful examination of the profiles and an elucidation of the complex physical processes during melt. This is explained in section 3 with a detailed discussion of processes during melt. The boundaries determined in section 3 are shown in Figures 4 and 5.

The position of the *ocean interface* can be estimated from temperature profiles alone as long as sea ice and ocean temperature are different. The ice-ocean interface can typically be estimated with a 2-cm accuracy (Provost et al., 2017). The method works from the beginning of the record until the end of June as sea ice is colder than the ocean. From 15 August to the end of the record, the whole sea ice layer is warmer than

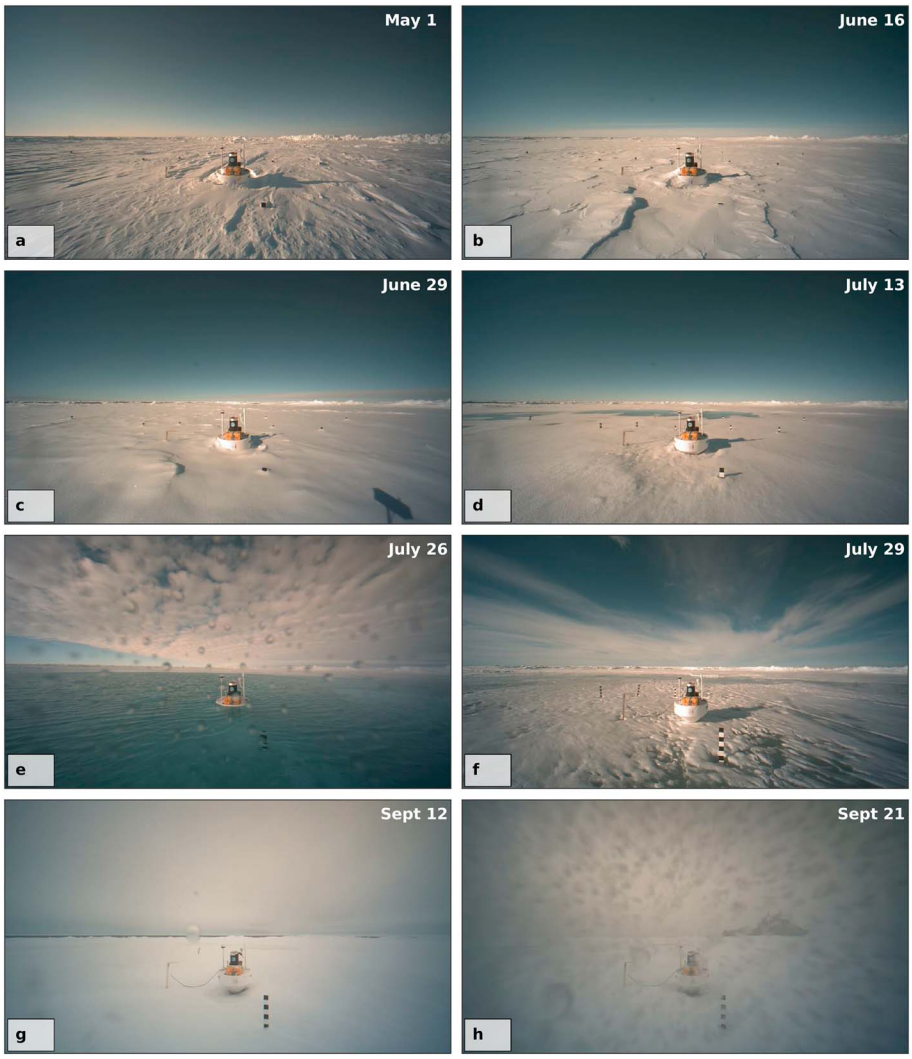

Figure 3. Webcam images from site A: (a) 1 May at 10:12: a ridge formed to the right. (b) 16 June 16 at 8:32: maximum snow thickness of 0.60 m at the sea ice mass balance for the Arctic. (c) 29 June 29 at 8:14: snowmelt started. A lead opened in the background to the left. (d) 13 July at 7:40: puddles are observed at the surface in the background; lead still visible. (e) 26 July at 7:21: melt pond around the buoy at its maximum depth. (f) 29 July at 7:18: melt pond drained, puddles observed in the background. (g) 12 September at 17:41: after a storm, deposition of snow and opening of a lead in the background. (h) 21 September at 5/25: Icebreaker KV Svalbard in the lead before buoy recovery. Owing to the wide-angle lens used in the camera, the buoy and the stakes appear farther away than they are.

the ocean and the interface can be estimated from temperature alone with a 2-cm accuracy. From the end of June to mid-August, the lower part of the sea ice and the upper ocean are nearly the same temperature. The interface becomes a thick spongy layer (Feltham et al., 2006), the lower limit of which can be empirically "guessed" with an uncertainty of about ±4 cm from zooming into the ocean temperature range, profile by profile, guided by information from the time derivative and ΔT_{120s}. Indeed, ΔT_{120s} shows a sharp contrast at the upper ocean interface on several profiles (Figures 4d and 5d), helping interface detection. At site A, the melt pond drained out in the ocean on 27 July and the lower limit of the freezing fresh water sets the upper ocean interface (Figure 4).

The resulting interfaces are consistent with the temperature derivatives (vertical and temporal) and ΔT_{120s} (Figures 4 and 5). During the fully developed melt season, the sea ice structure is transformed with melt-water percolation, temporarily freezing forming fresh ice plugs, meltwater drainage, and other processes. Variations in ΔT_{120s} help support our interpretation. This is detailed in the following section.

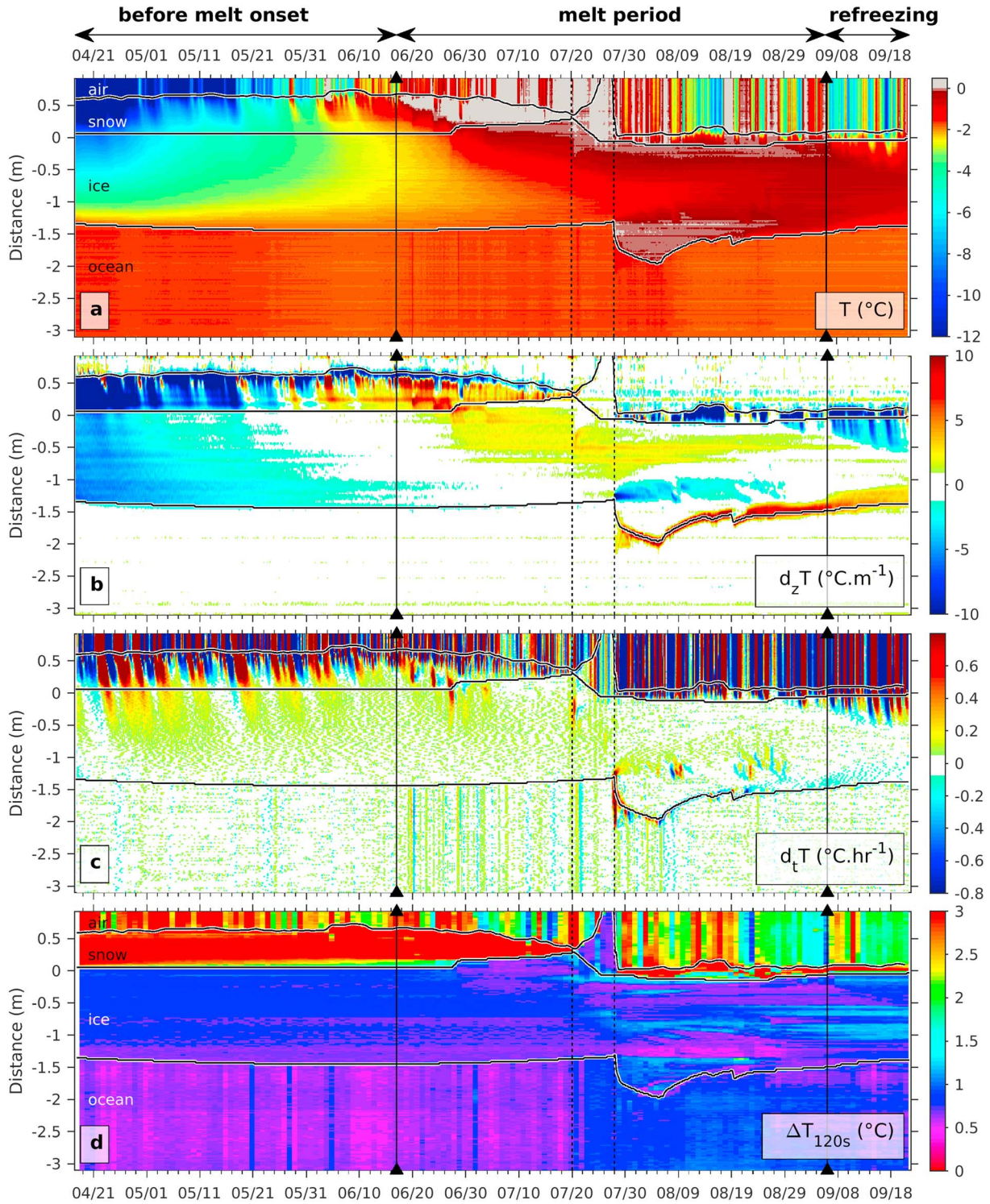

Figure 4. Data from sea ice mass balance for the Arctic at site A: (a) Temperature (°C). (b) Vertical derivative of temperature (°C/m). (c) Time derivative of temperature (°C/hr). (d) Heated temperature after 120 s, ΔT_{120s} (°C). *Y* axis is vertical distance (m) referenced to the initial snow-ice interface. Vertical resolution is 2 cm on all plots. Time resolution is 4 hr on the top three panels and 24 hr for the lower panel. Black and white isolines (24-hr running mean) correspond to the following main interfaces from top to bottom: lower limit of the atmosphere, upper limit of the sea ice, and upper limit of the ocean. Vertical lines mark the snowmelt onset (17 June) and the onset of refreezing (6 September). Dashed vertical lines mark the melt pond period (20–27 July).

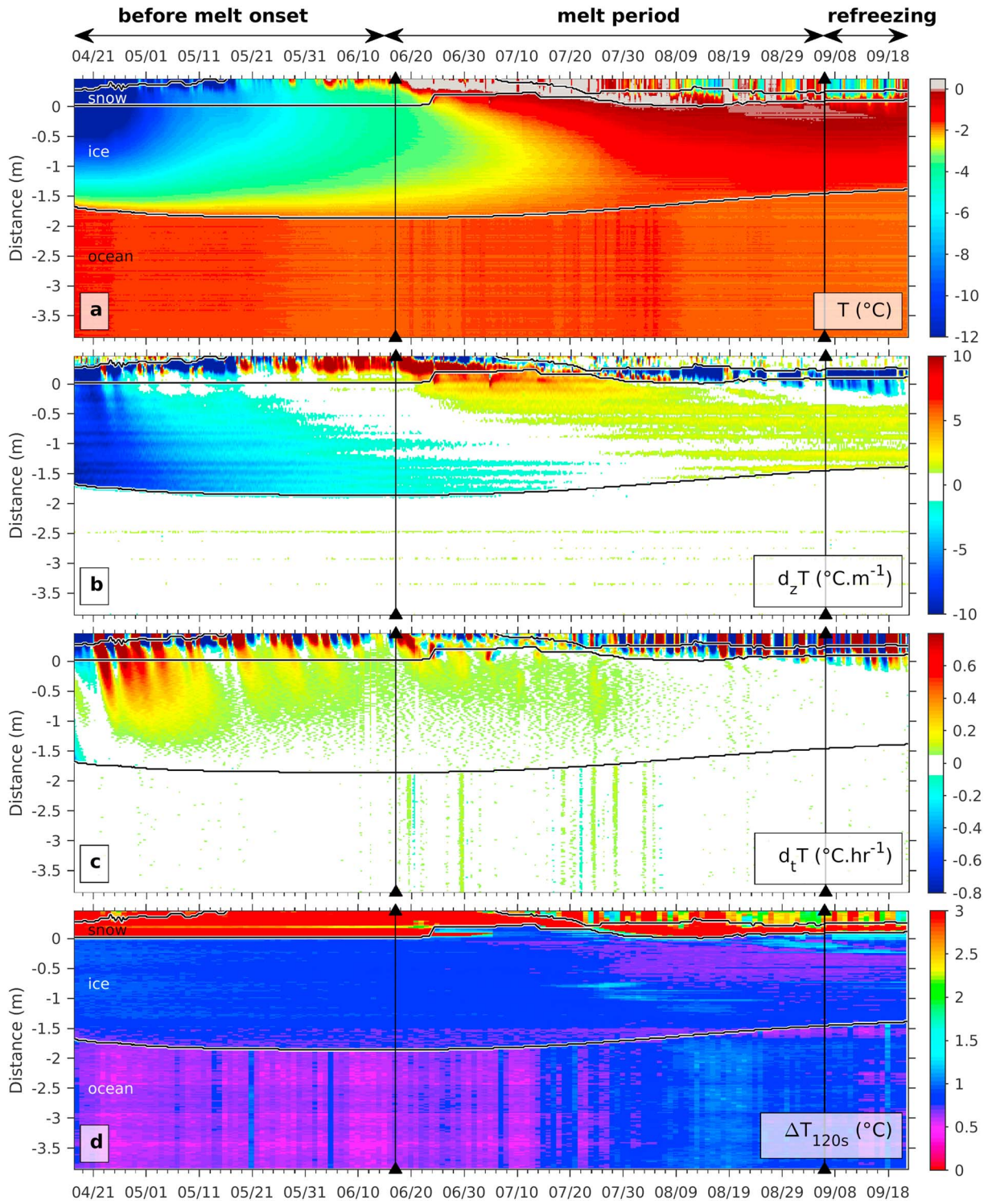

Figure 5. Same as Figure 4 for site B except that the time resolution is 6 hr for the top three panels.

3. Evolution of Snow and Ice at Sites A and B During the Drift

Three main periods are distinguished: prior to snowmelt onset, the melt period, and refreezing. Snowmelt onset was chosen as the date when positive temperatures are first observed in the snow (Figures 4 and 5). This occurred on 17 June when air temperatures were still negative, apart from a short stormy episode

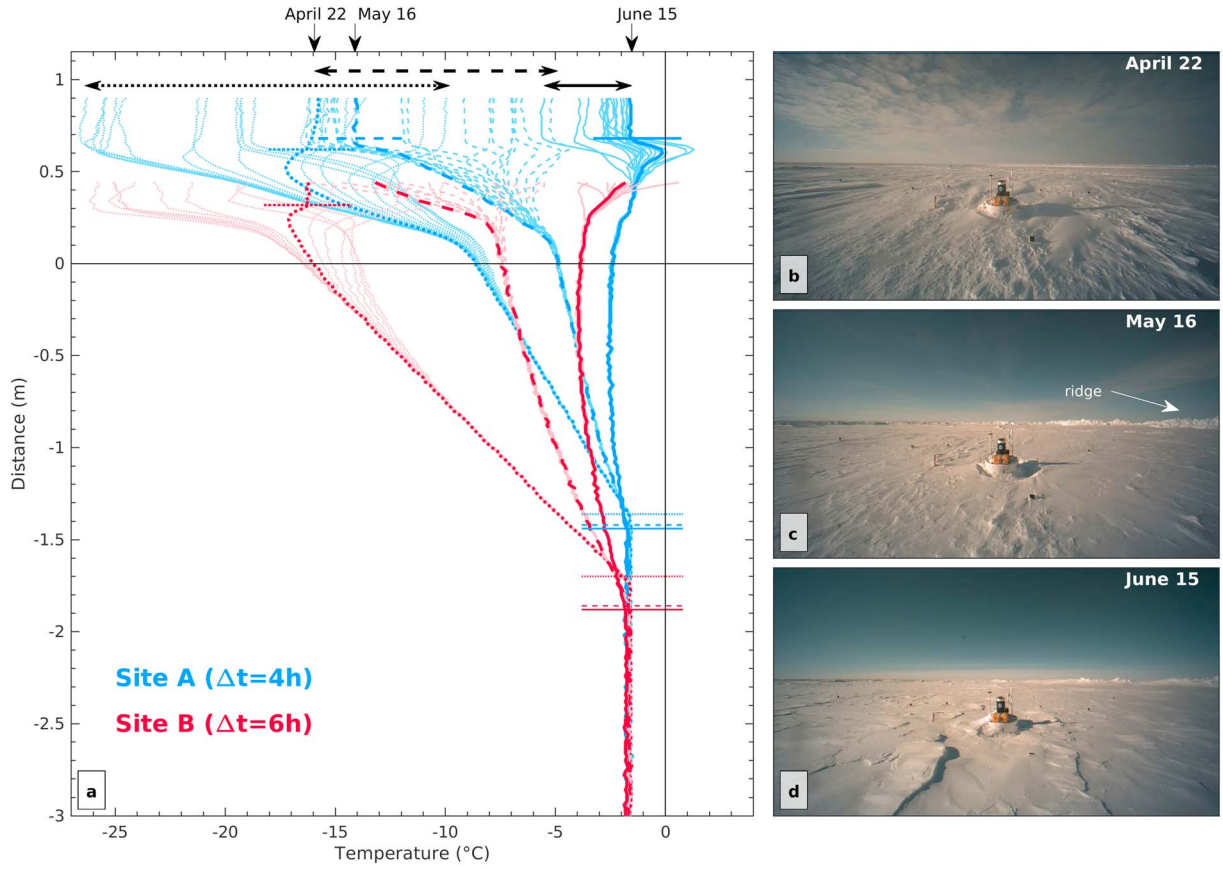

Figure 6. (a) Selected temperature profiles before melt onset from site A in blue (site B in red) and corresponding webcam images from site A. Selected dates are (b) 22 April, thick dotted lines, (c) 16 May, thick dashed lines, and (d) 15 June, thick full lines. Interfaces are marked for the corresponding date. The 18 (12 for site B) profiles from 3 days centered at the date of the image are shown in light blue (light red). The horizontal arrows above the profiles indicate the air temperature range over 3 days. *X* axis is temperature (°C), and *Y* axis is distance (m) from the initial ice-snow interface.

with positive air temperatures on 4 June (Figure 2b). Positive air temperatures were frequently observed from 23 June to 6 September, the exception being a week in August. The refreezing period (continuously negative air temperatures) started on 6 September, and the instruments were recovered on 21 September.

3.1. Until Snowmelt Onset: From 21 April to 16 June

Air temperature ranged from −27 °C on 21 April to above zero in early June (Figure 2b). Its variations were strongly affected by storms. Storm-associated warm air temperatures were higher than snow and sea ice temperatures and triggered high-temperature pulses that diffused down into the snow and ice (Figures 4 and 5). Those pulses stand out in the temperature time derivative during the premelt period (Figures 4c and 5c). Snow deposition and rain episodes were consistently observed in the webcam and in the SIMBA records at site A: they often coincided with the beginning of a storm. A major snow event on 4 June led to a snow depth increase from 0.55 to 0.65 m at site A. At site B, snow depth increased gradually from 0.22 m on 21 April to more than 0.40 m on 18 May. The SIMBA chain at site B was buried in snow from 18 May to 4 July.

Ice thickness first increased from 1.42 to 1.52 m at site A and from 1.72 to 1.92 m at site B. The maximum thickness was reached about mid-May at both sites. The larger ice growth at site B (0.20 m versus 0.10 m) is consistent with smaller snow depth during the cold period (until 16 May) and, therefore, less insulation from snow than at site A.

Temperature profiles centered on 22 April (Figure 6a, red and blue dotted line profiles) illustrate the large air temperature variations (range of about 16 °C) and the insulation effect of snow on temperature variations between sites A and B (1 °C versus 3 °C amplitude at the snow-ice interface and 0.30- versus 0.80-m

penetration in the ice). As a result, ice was colder at site B compared to site A (by about 7.5 °C at the snow-ice interface).

Temperature profiles centered on 16 May (Figure 6a, dashed line profiles) show, compared with the 22 April data, a reduced range in air temperature variations (less than 10 °C), thicker snow layers (+0.08 m at site A, >+0.15 m at site B), reduced temperature variations in the snow (almost none at the snow-ice interface), and thicker (+0.08 m at site A and +0.17 m at site B) and warmer ice with a quasi-linear temperature profile (from ocean temperature to −7.6 °C at site B and to −5 °C at site A). Note the presence of a ridge on the corresponding webcam image from 16 May (Figure 6c).

At the end of the pre–snowmelt period, on 15 June, the two sites were at 86.2°N and 2.2°W (Figure 2a). Temperature profiles at this time show a reduced temperature range (5 °C in the atmosphere), a minimum temperature in the sea ice at about 0.50 m below the snow-ice interface (−2.7 °C at site A and −4 °C at site B) and thicker ice (+0.10 m at site A and +0.20 m at site B; Figure 6a, full-line profile). The corresponding webcam image shows the snow depth increase (+0.10 m) next to the buoy (ablation stakes are hardly visible) and the snow-smoothed slopes of the ridge (Figure 6d compared to 6b). During this period, no signs of melt are seen at the surface while temperature changes in the sea ice are important.

3.2. Surface Melt Period: From 17 June to 6 September

We divided the melt period at the SIMBAs into three parts: the snowmelt period from 17 June to 20 July (section 3.2.1), the site A melt pond period from 21 to 27 July (section 3.2.2), and the period after site A melt pond draining from 28 July to 6 September (section 3.2.3).

The webcam images confirm snow melting (identified with positive temperatures in the snow) in the second part of June: the snow surface is smoother on 29 June (Figure 3c) than on 16 June (Figure 3b). The first small water puddles appeared around 10 July in the background at site A (e.g., Figure 3d). Air temperatures often above zero during July (Figure 2b) facilitated a massive snowmelt with snow thickness dropping to zero by 20 July at both sites. The SIMBA chains (sites A and B) document snowmelt (Figures 4, 5, and 7). At site A, the instruments were at a low location on the floe where meltwater accumulated and reached over 1.20 m in height above sea ice on 27 July (Figure 3e). Then within a dozen hours, the melt pond drained out (Figure 3f). The SIMBA data document the release of fresh water into the ocean and its freezing into a false bottom (Figures 4 and 8). Site B was at a high location on its floe. As a result, meltwater did not accumulate; it either percolated through the ice or flowed downward.

3.2.1. Snowmelt Period: From 17 June to 20 July

On 17 June, snow was 0.60 m thick at site A (>0.40 m at site B where the SIMBA was buried in snow; Figures 7c and 7d) and internal melt started soon after. A maximum in temperature is observed about 8 cm below the snow surface as documented in the temperature vertical gradient (Figures 7e and 7f). Webcam images illustrate snowmelt at the surface (Figures 3b and 3c). Snow also melted from within, with meltwater dripping down through the snow until it encountered temperatures cold enough to cause it to freeze. This percolation occurred step by step, deeper and deeper in the snow, as clearly seen in the temperature time derivative (Figures 7g and 7h, 20, 24, and 27 June at both sites). Water slightly above 0 °C percolated down (positive time derivative) and refroze (negative time derivative). As temperature increased in the snow, meltwater percolated through the entire snow layer and reached the ice surface (27 June at site A and 5 July at site B) where it partially froze to form superimposed/slush ice (Figures 7a, 7b, and 8a). The snow was melted out at site A by 20 July, while site B reached a minimum snow depth (0.04 m) on 23 July (Figures 7 and 8b).

Superimposed/slush ice showed temperatures between −1 and +0.5 °C, indicating that it contained water pockets (Figures 7c and 7d). About 0.2 m of superimposed/slush ice was observed at both sites on 5 July. At site B, the thickness of the superimposed/slush ice diminished by 0.05 m on 15 July following a rain episode as if the top part of the superimposed ice (still below 0.10 m of wet snow) flowed down into lower parts of the floe. In contrast, the superimposed ice thickness at site A did not change (0.20 m).

During the snowmelt period, sea ice warmed up and began to thin from below probably from melting as the ocean was still warmer than the sea ice base. On 30 June, sea ice (including superimposed ice) was 1.53 m thick at site A (2.05 m at site B) and had a temperature minimum of −2.1 °C (−3.0 °C at site B) at 0.90 m below the ice-snow interface (not shown). Profiles on 5 July 5 (Figure 8a; thicknesses slightly smaller and

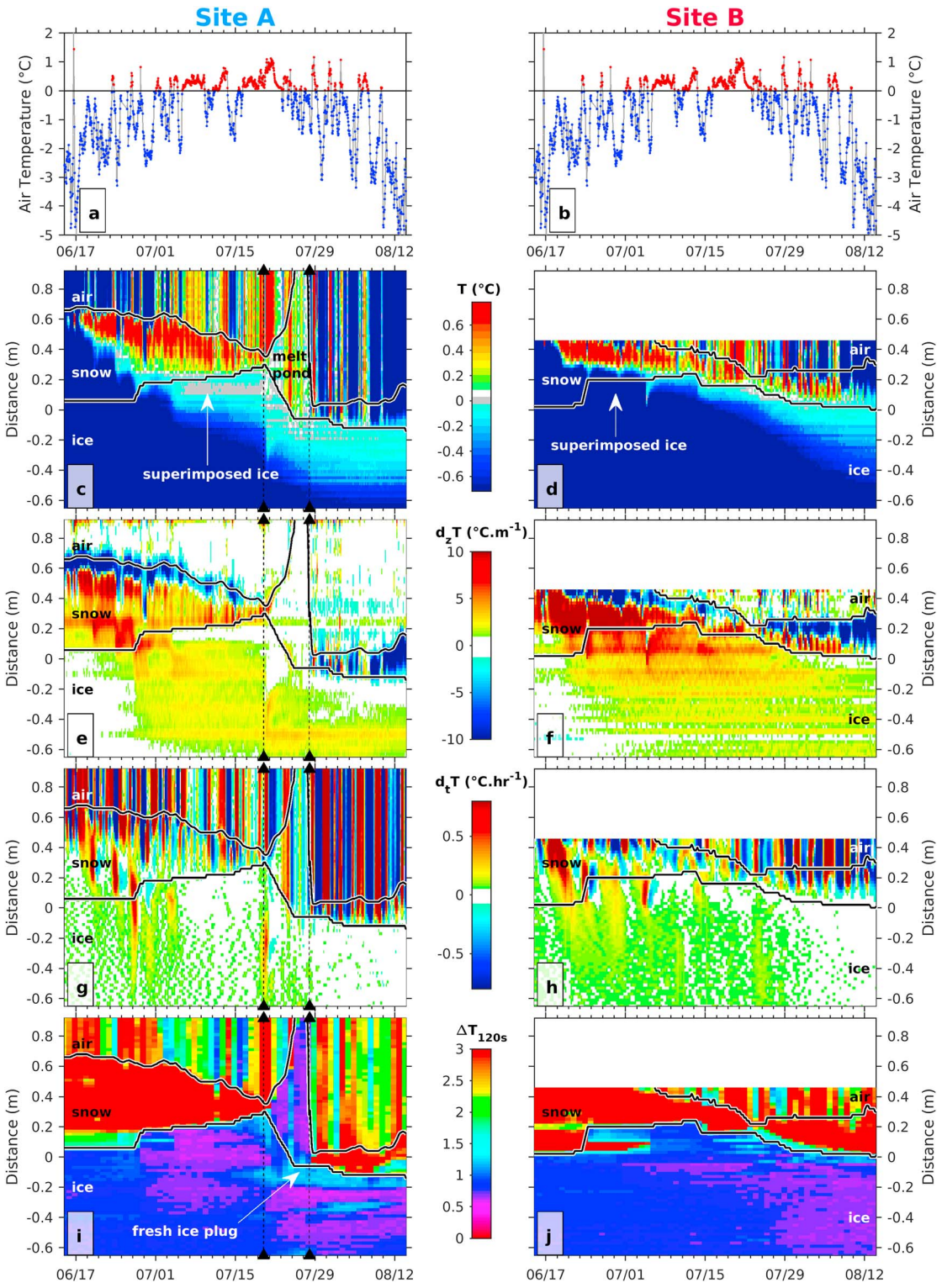

Figure 7. Close-up from mid-June to mid-August on the upper interfaces: snowmelt, melt pond building, and apogee at sites A and B. The two top panels (a and b) are the same air temperature close-up from central unit at site A (time resolution 1 hr; temperatures above 0 °C in red). (c) Temperature from sea ice mass balance for the Arctic (SIMBA) (°C) at site A. (d) Same at site B. (e) Vertical derivative of temperature (°C/m) at site A from SIMBA. (f) Same at site B. (g) Time derivative of temperature (°C/hr) at site A from SIMBA. (h) Same at site B. (i) Heated temperature (°C) after 120 s at site A from SIMBA. (j) Same at site B. *Y* axis is vertical distance (m) referenced to the initial snow-ice interface. *X* axis is time (ticks every 2 days). Vertical resolution is 2 cm on all plots. Time resolution is 4 hr for site A (6 hr for site B) for the SIMBA temperature and derivatives and 24 hr for the lower panels (ΔT_{120s}) for both sites. Black and white isolines correspond to interfaces: between atmosphere, "old" sea ice, sea ice, superimposed ice, and melt pond as labelled. Dashed vertical lines mark the melt pond period (20–27 July).

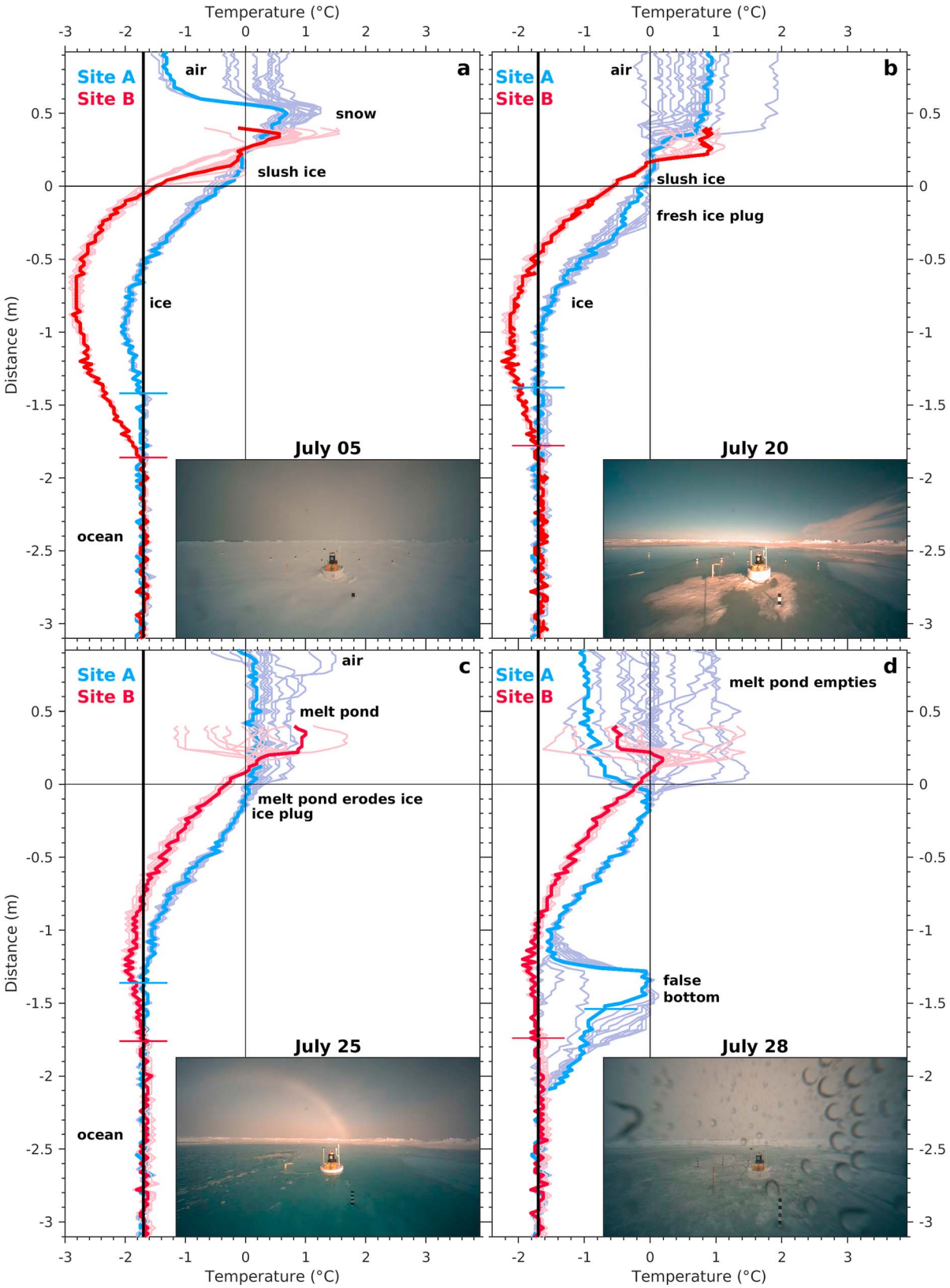

Figure 8. Selected temperature profiles during the melt period from site A in blue (site B in red) and corresponding webcam images on (a) July 5. (b) July 20. (c) July 25. (d) July 28. The 18 (12 for site B) profiles from 3 days centered at the date of the image are shown in light blue (light red for site B). *Y* axis is distance (m) from the initial ice-snow interface.

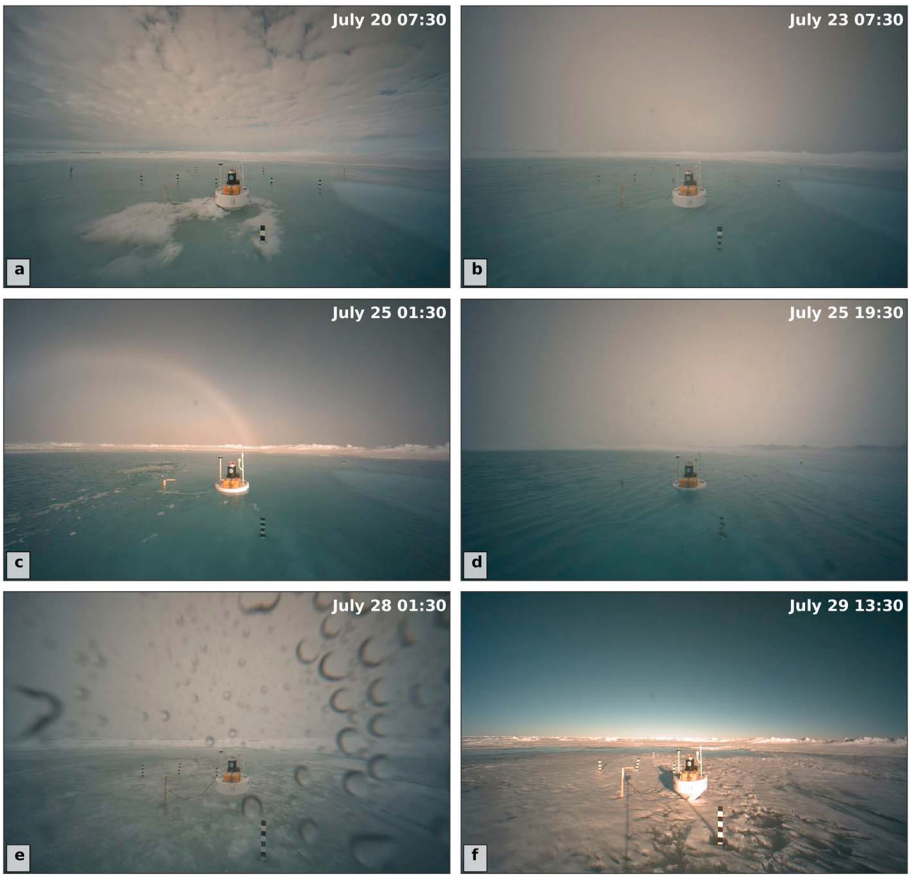

Figure 9. Pond in the webcam images. (a) 20 July at 7:35: Meltwater close to sea ice mass balance for the Arctic (SIMBA). The buoy is above a snow dune, the SIMBA is still seeing snow. (b) 23 July at 7:32: No more snow in the vicinity of the SIMBA. (c) 25 July at 1:19: Pieces of super imposed ice are seen at the surface 3 days before the pond empties. (d) 25 July at 19:25: Melt pond at its maximum. Waves at the surface. (e) 28 July at 1:13: Just after pond drainage. The buoy is lifted up by 20 cm. (f) 29 July at 13:12: Buoy sitting back in the ice. Puddles and remnants of the pond are seen in the back in a depression of the floe topography.

temperatures slightly warmer than on 30 June) show a layer of meltwater at 0 °C just above the initial snow-ice interface at both sites below the remaining warm and wet snow. This meltwater layer was 0.20 m thick at site A (blue profiles) and 0.10 m thick at site B (red profiles).

At site A, on 20 July, the ice thickness (including 0.20 m of superimposed ice) was about 1.65 m and the sea ice temperature was equal to or larger than the ocean temperature (Figure 8b, blue profiles). On 19 July, water at 0 °C infiltrated down to 0.30 m into the ice and froze, creating a fresh ice plug (Figure 8b, light blue profiles). The fresh ice plug (or interposed ice) sealed the ice against percolation and allowed water to pool above it (e.g., Polashenski et al., 2017). Snow was melted out, and a water layer grew to about 0.35-m height above the initial snow-ice interface (Figure 8b, blue profiles).

At site B, the ice thickness (including 0.15 m of superimposed ice) was 1.95 m ($\Delta h = -0.10$ m), the sea ice temperature showed a minimum of −2.1 °C at 1.40 m below the initial ice-snow interface, and there was hardly any water above the initial snow-ice interface (Figure 8b, red profiles). The meltwater either infiltrated sea ice and/or flowed away downslope.

In summary, during the snowmelt period, sea ice has thinned from below (of about −0.1 m at both sites), been capped with superimposed/slush ice (+0.20 m decreasing to 0.15 m at site B), and warmed significantly. At site A, on 20 July, the sea ice was warmer than the ocean (Figure 8b).

3.2.2. Melt Pond Period: 20–27 July

The site A buoy was on top of a snow dune (Figure 9a) at a low location on the floe, and meltwater accumulated in the buoy vicinity (Figures 3e, 9b, and 9c). The melt pond built up around the buoy and reached a depth exceeding the buoy flotation height (1.20 m). Water reached the top of the buoy (Figure 3e) and

managed to lift it up by about 0.20 to 0.30 m as seen in the webcam picture taken just after the pond drainage (27 July; 1:13 UTC, Figure 9e). Twelve hours later, the buoy flotation was back on the ice and remnants of the melt pond can be seen in the background at lower locations of the floe (Figure 9f). The webcam documents heavy rain at the time of the pond maximum.

The SIMBA data show that as the melt pond rose, the ice surface warmed (Figure 7c). Three days before the pond drainage (25 July), superimposed ice detached. Pieces of ice are seen at the pond surface (Figure 9c). Temperatures in the melt pond were homogeneous in the vertical and showed a daily cycle ranging from 0.3 to 0.8 °C (Figures 7c, 7e, 7g, and 8c). This homogeneity is probably due to wind mixing: ERA-I indicates wind speeds in excess of 5 m/s (Figure 2c), and the webcam shows wavelets at the pond surface (Figures 9b–9d). The pond water absorbed radiation and was warmer than the air on 27 July, a cold sunny day (Figure 8c). The well-mixed pond water led to about 0.20-m ice surface ablation in 3 days (Figure 7e). When the pond reached its maximum height, the ice was thin (1.25 m) and warmer than the ocean (Figure 8c). The entire sea ice layer showed temperatures above −2 °C, and the sea ice should be highly permeable (Golden et al., 2007), although we do not have salinity observations to prove it.

In agreement with Polashenski et al. (2017), the presence of fresh ice plugs explains why a warm and permeable sea ice can support a 1.20-m-deep pond. Fresh water infiltrated the highly porous ice and temporarily froze (cf. 19 July, described above). The temperature profiles, for example, those centered on 25 July, show homogeneous meltwater until distance 0, a time changing slope between 0 and −0.1 m associated with the pond digging the ice and a constant slope of 0.4 °C/0.3 m between −0.1 and −0.25 m corresponding to a freshwater ice plug (Figure 8b, light blue profiles). The heated temperature (ΔT_{120s}) indicates discontinuities consistent with the temperature profiles. Empirically, this ice plug area corresponds to ΔT_{120s} of about 1.35 °C (Figure 7i), and ΔT_{120s} values below 0.5 °C correspond to water or slush ice (Figures 7i and 7j).

In contrast, meltwater depth at site B never exceeded 0.10 m (Figure 8c, red profiles, in the distance range 0.1–0.2 m). Meltwater percolated in the ice or flowed away toward lower locations. The upper limit of the superimposed/slush ice remained at around +0.13 m (Figures 7h and 8c, red profiles) until 25 July. By 25 July, the ice thickness (not including superimposed/slush ice) reduced to 1.71 m. The ice showed temperature larger than −2 °C and even above −1.7 °C (the ocean temperature) in the upper meter where the ice was not in direct contact with the ocean.

3.2.3. 28 July to 5 September: Under-Ice False Bottom (Site A), Continuous Basal Melt (B)

At a time of heavy rainfalls and strong southerly winds, the pond at site A drained in less than 6 hr on 28 July, probably through a drainage hole whose remnant was found 3 m away from the SIMBA chain as explained in section 3.3; however, there might have been other cracks. The fresh meltwater which outpoured into the ocean had a temperature just above 0 °C and being lighter than the cold and salty sea water formed a thick layer of fresh water sandwiched between colder old sea ice and colder sea water (Figure 8d blue profiles and Figure 10). Because heat conduction occurs more rapidly than salt diffusion, the fresh water cooled to its freezing point and fresh ice formed quickly in the newly formed under-ice pond. The outer limit is marked with a local extremum in temperature time derivative (amplitude above 0.5 °C/hr) that changes sign at the thickness maximum (Figure 10b) and with a clear maximum in the vertical derivative (Figure 10c).

Notz et al. (2003) analytical model predicts that the squared ice thickness, h^2, is proportional to time: $h^2(t) = 4\,D^*\,t$, where D^* is a diffusion-like coefficient (see details in Appendix A). We estimated D^* from the thickness h. Here, the growth during the first 24 hr followed this law with a constant of proportionality of about 65 cm^2/hr providing an estimate for D^* of 4.5×10^{-7} m^2/s. Then the regime changed, and, during the following 7 days, the same law applied with a constant of proportionality reduced to 15 cm^2/hr corresponding to a D^* of 10^{-7} m^2/s. The ice thickness growth, with about 0.65 m of fresh ice produced in 10 days, was much faster than in the quiescent laboratory experiments described by Martin and Kauffman (1974), who reported a much smaller nonturbulent diffusion coefficient of 7.5×10^{-10} m^2/s. The fresh ice growth is discussed in more detail in Appendix A. Inside the ice envelope, thin layers with temperatures above zero suggest the existence of fresh water pockets (Figure 10a). Note that during the fresh ice growth, the drift velocities were mostly below 0.15 m/s (Figure 10f).

After 8 August, the new ice thickness decreased from 0.65 to 0.10 m in 10 days: salty seawater eroded the fresh ice. Ablation was caused by dissolution rather than melting (Notz et al., 2003; Woods, 1992). During this period, drift velocities were large, often above 0.2 m/s and reaching up to 0.3 m/s, with semidiurnal

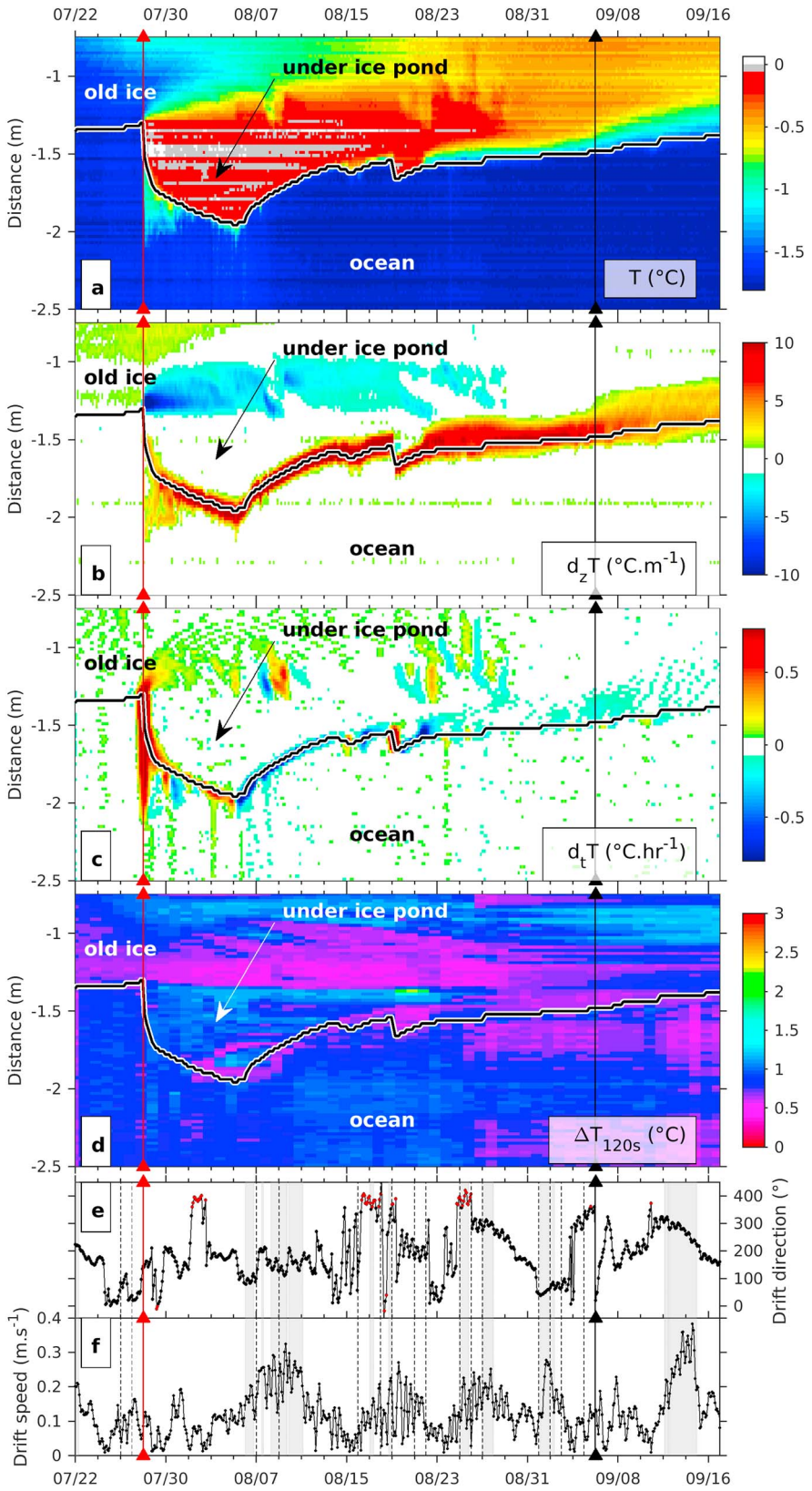

Figure 10. Close up on the sea ice bottom after melt pond draining: site A. (a) Temperature (°C). (b) Vertical derivative of temperature (°C/m). (c) Time derivative of temperature (°C/hr). (d) Heated temperature after 120 s ΔT_{120s} (°C). (e) Drift direction (degrees north is 0 and east 90). (f) Drift speed (m/s). Date of meltwater drainage is in red and date of freeze onset in bold black (as in Figures 2b–2e).

variations indicative of inertial wave activity (Figure 10f). These motions probably enhanced the dissolution. The underpond thickness increased again by 10 cm on 18/19 August after a few days of above zero air temperatures and heavy rainfalls seen in the webcam images. This suggests that the rainwater was drained into the ocean, possibly through the same drainage hole (see section 3.3). Erosion then resumed, the bottom of the freshwater ice migrated upward, and the ice bottom reached its former level by the beginning of September.

The "old" sea ice, colder than the newly formed fresh ice, was heated from below (Figures 10a and 10c with $dT/dz < 0$ in the depth range −1.0 to −1.45 m from 28 July to 29 August) and partially melted. Low ΔT_{120s} values below 0.5 °C in the range −1.10 to −1.30 m just above the fresh ice (Figure 10d) empirically correspond to slush ice. The temperature time derivative indicates sporadic events in the slush (7–11 August and 19–23 August; Figure 10c) occurring at times of heavy rain and large drift speed (Figure 10f). The precise nature of these events is not known.

During the false bottom period, the old sea ice was heated from above and below and the temperature profiles show a minimum that warmed from −1.5 °C at −1.1 m (July 28) to −0.9 °C at 0.90 m (29 August; Figures 4a, 8d, and 11a blue profiles). By 5 September, the ice showed temperatures between −0.5 and 0 °C (Figure 11b, blue profiles).

In contrast, at site B during the same period (28 July 28 to 5 September) the sea ice experienced continuous basal melt, losing about 0.26 m in 5 weeks, while the ocean was colder than sea ice (Figures 5, 8d, and 11b).

At both sites, alternating snow and rain episodes and occurrences of positive air temperatures that melted the snow, induced more surface freshwater that percolated in the ice, warmed it up and refroze (examples 19 August or 3–7 September; Figures 5a, 5b, and 11b). Temperature profiles on 5 September show similar locations for the ice ocean interface at the two sites, a surface ice erosion of 0.20 m at site A (0.02 m at site B) and colder temperatures at site B in the lower meter of ice and similar temperatures above (Figure 11b).

3.3. Refreezing Period: 6–21 September (Date of Recovery)

At the beginning of the refreezing period (continuously negative air temperatures in Figure 2b), ice, snow, or water alternately covered the webcam lens and visibility was poor. SIMBA profiles centered on 9 September show a large range in air temperatures and a difference in sea ice temperatures between sites A and B (Figure 11c). The ocean was found at −1.45 m below the initial ice-snow interface at both sites, and sea ice temperatures were still larger at site A at depth below 0.4 m due to the heat brought by the pond drainage 38 days earlier. At the end of the records, the ice base was at its initial location (1.40 m) at site A, whereas at site B it was up by 0.30 m (from 1.70 to 1.40 m; Figure 11d). Ice temperature was above ocean temperature at the two sites, with ice temperatures at site A being lower than at site B near the surface and higher in the lower part (Figure 11d).

On 12 September (Figure 3g), the webcam showed a thin cover of snow and the wide-open lead in the background. The KV Svalbard used the lead to approach site A (Figures 3h and 11d). At recovery on 21 September, the water-worn surface of floe A suggested past erosion from water streams converging toward a drainage hole found next to the buoy 3 m away from the SIMBA (Figures 12a, 12b, 12c, and 12d). Hot water from the ship (used to weaken the ice around the buoy to ease recovery) followed the same path. The ice surface was made of fresh ice. Pictures taken during recovery confirmed the layered structure of the floe as suggested by ΔT_{120s} (Figure 12e): below a thin snow cover (0.10 m), layers of fresh consolidated ice alternated with more porous ice. In spite of 0.10 m of superimposed ice formed after rain and snowmelt episodes late August, the snow-ice interface was 0.10 m lower than its initial position at site A.

At site B, the snow-ice interface was 0.08 m above its initial position as a result of snow deposition, melting and rain that refroze (Figures 11 c and 11 d, red profiles). A layer of 0.15 m of snow covered 0.30 m of fresh solid ice (-0.5°C), then temperature decreased linearly toward ocean temperature. Recovery took place during a foggy evening and the few clear moments showed that the floe was flat (Figure 12f).

4. Discussion

In this section we summarize the evolution of thicknesses of snow and ice all along the drifts and discuss ice desalination, structure transformation, and topography.

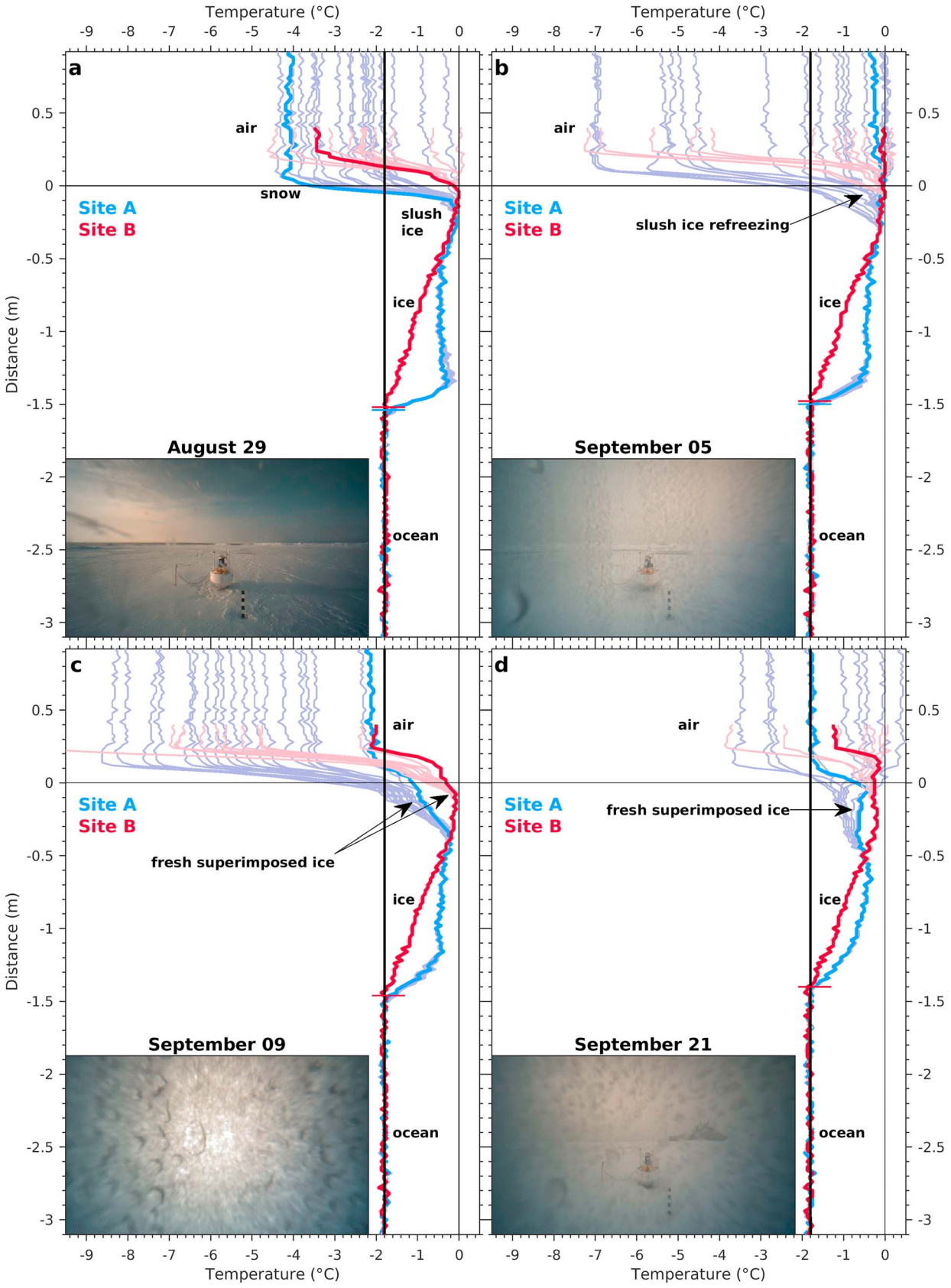

Figure 11. Same as Figure 8 on (a) 29 August. (b) 5 September. (c) 9 September. (d) 21 September.

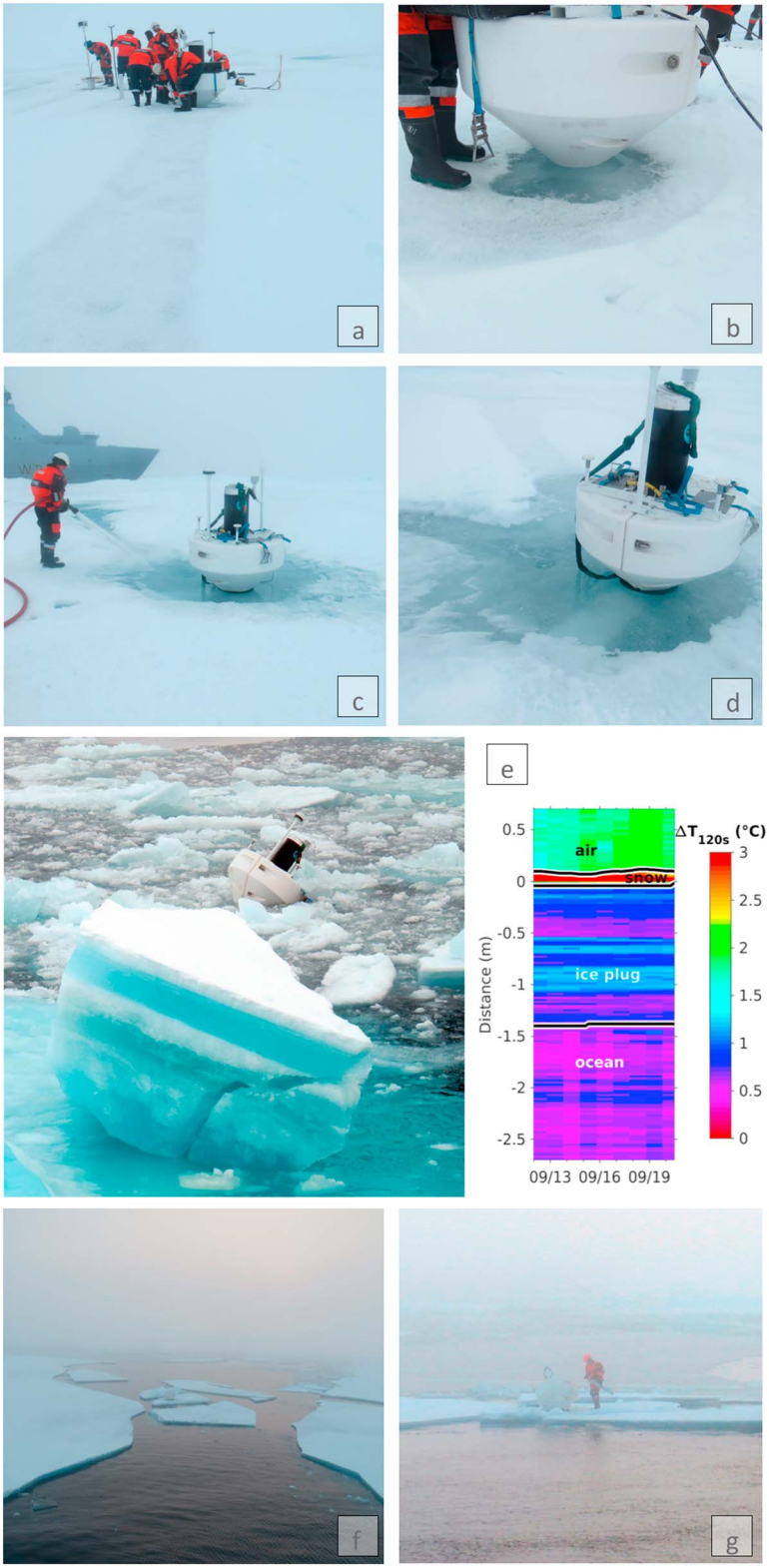

Figure 12. Photographs taken during recovery on 21 September 2013: (a) Site A: erosion due to water streams leading to the buoy. (b) Site A: buoy resting on fresh water ice. (c) Site A: flushing warm water (to ease buoy recovery) reveals drainage hole next to the buoy (KV Svalbard in the lead in the back). (d) Site A: close up on drainage hole. (e) Site A: piece of floe broken during recovery: layering with freshwater ice and salt water ice consistent with ΔT_{120s} profile. (f) Site B: broken floe (due to icebreaker) foggy conditions. (g) Site B: close-up on the broken floe.

4.1. Evolution of Thicknesses Over the Summer

The evolution of snow depth and of the different contributors to ice thickness (superimposed ice, surface ice ablation, and evolution of the ice base) is summarized in Figure 13a.

At site A, the initial snow depth was 0.52 m, which increased to 0.66 m on 10 June (Figure 13b). Then it decreased and snow was melted out by 20 July. At site B, snow had an initial depth of 0.22 m, then completely covered the chain (thickness >0.45 m) from 15 May to 5 July. Snow was almost melted out by 23 July (less than 0.04 m left). Snow alternately accumulated (up to 0.30 m by mid-August at both sites), melted, and stabilized to about 0.15 m after 10 September at both sites.

The superimposed ice (Figure 13c) that formed (about 0.2 m at each site) in late June during the snowmelt was lost in July. After 1 August, alternating precipitation, melt, and freeze events eventually led to persistent superimposed ice (about 0.1 m thick at each site) by 1 September. Erosion of the ice surface was larger at site A. The melt pond-enhanced erosion led to a surface ablation of 20 cm in 3 days. The final ice surface was lower than the initial one by 0.10 m (in spite of the 0.10-m-thick superimposed ice) at site A, while the final ice surface at site B was 0.1 m higher than the initial one.

During the cold period, basal ice growth was larger at site B (0.20-m site B versus 0.10-m site A), which also had less snow cover than site A (Figure 13e). Basal ice growth stopped between 20 and 26 May. Basal ablation started between 24 and 26 June at both sites and continued monotonously at site B until the end of the time series. Site B lost 0.50 m from basal ablation. With such a basal ablation, site A (blue dashed line on Figure 13e) would have ended with 0.9 m of sea ice instead of 1.40 m. The difference between the actual ice-ocean interface and the hypothetical interface obtained using site B ablation (blue dashed line in Figure 13e) gives an estimation of the contribution of the false bottom to thickness (Figure 13f). This calculation provides an estimated false bottom thickness of 0.40 m at the end of the record (Figure 13f). About 0.30 m of false-bottom fresh ice was lost from dissolution in a week (7–5 August). The dissolution was less effective after 15 August, perhaps due to the presence of a thin layer of relatively fresh water underplating the ice as suggested in the record of ΔT_{120s} (Figure 10d). There were no drastic changes in ice drift velocity amplitudes, which often exceed 0.2 m/s (Figure 10f).

4.2. Ice Desalination, Structure, and Topography

The data suggest strong ice desalination (which was not measured as no ice cores were taken). Values of ΔT_{120s} indicated frost on the SIMBA chain in the ocean starting on 22 July at site A (20 July at site B) at a time of intense basal melt and lasting until 25 August (Figures 4d, 4e, 5d, and 5e). We interpret this frost as a result of cold brines flushed down as the surface fresh meltwater percolates downward in the ice and displaces the resident high salinity brines. The cold brines, below local freezing temperature, facilitated water freezing along the chain leading to frost. In support of this interpretation, note the corresponding negative time derivative of the ocean temperature on 22 July at site A (20 July site B; Figures 4c and 5c) and the small drift velocities at these dates (Figure 2c) that cannot account for the change in ΔT_{120s}, which is sensitive to motion (Jackson et al., 2013). The frost near the ice went away when a layer of relatively light freshwater underplating the ice developed (as suggested in ΔT_{120s} in Figures 4d and 5d).

The photographs from recovery show flat floes at both sites (e.g., Figures 12f and 12g). Values of ΔT_{120s} suggest layered structures with "blue values" corresponding to fresh consolidated ice and "pink values" corresponding to more porous ice (Figures 4d and 5d). At site A, remnants of fresh consolidated ice (the ice plugs or interposed ice) were sandwiched between blue layers of old ice (Figures 12e and 4d).

Sketches in Figure 14 illustrate a possible scenario for the evolution of the snow and ice on the floe at site A from 15 June at the onset of snowmelt to 6 August at the maximum thickness of the false bottom. This scenario is consistent with the observations. The webcam saw puddles and a lead, whereas the SIMBA recorded superimposed ice on 15 June (Figure 14a). On 25 July, the melt pond was large and superimposed ice detached from the bottom was seen floating at the pond surface (Figure 14b). The sea ice absorbed fresh meltwater, and fresh ice plugs supported the pond. The weight of the pond deformed the warm and elastic sea ice into a more concave shape. The pond drained out in the ocean on 27 July through a drainage hole 3 m away from the SIMBA, and fresh ice rapidly formed (see Appendix A; −0.65 m in 10 days) below the old ice

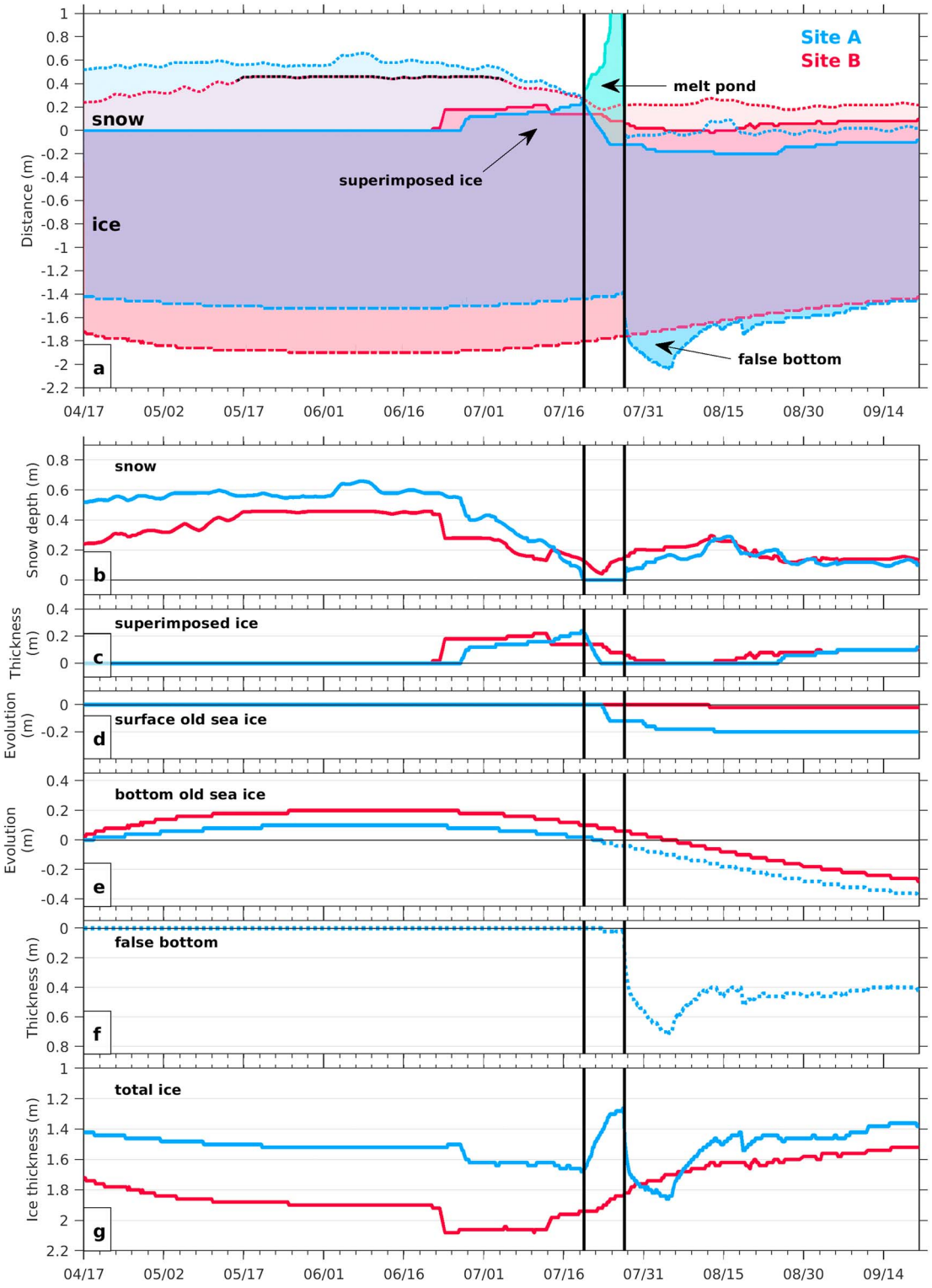

Figure 13. Along trajectory time series of thicknesses (m). Values for site A in blue and for site B in red. The black vertical lines correspond to the melt pond period. (a) Superposition of the interfaces (air-snow, snow-ice, ice-ocean) at the two sites. Y axis is the distance to the initial snow-ice interface. The air-snow interface at site B is above the black dots (and not precisely known) between May 15 and July 5 (sea ice mass balance for the Arctic chain entirely buried in snow). The melt pond surface is shown in turquoise. (b) Snow depth. The red dashed line is the lower limit of the unknown snow thickness. (c) Superimposed ice thickness. (d) "Old sea ice" surface evolution relative to its initial value. (e) Old sea ice bottom evolution relative to its initial value. The dashed part of the blue line corresponds to an extrapolation from site B. (See text). (f) False bottom thickness estimate at site A (vertical axis is upside down). (g) Total ice thickness (vertical axis is upside down).

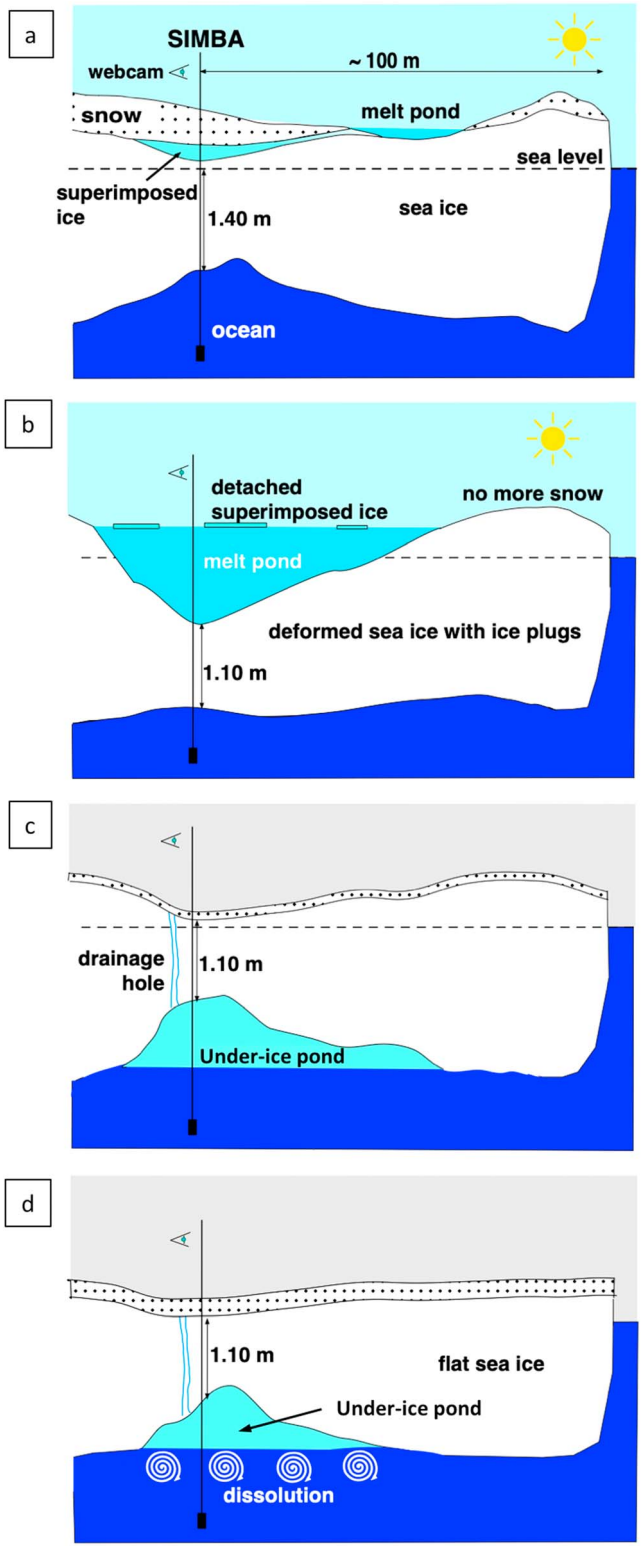

Figure 14. Floe topography sketches site A. (a) 13 July: snowmelting, superimposed ice, puddles, and a lead in the background. (b) 25 July: melt pond growing, floe deformation, and detached superimposed ice at the pond surface. (c) 30 July: meltwater poured out into the ocean through a drainage hole freezes under the sea ice. (d) 12 August: turbulence-enhanced dissolution of the fresh ice.

(Figure 14c representing 4 August). Then dissolution, enhanced at a time of high drift speeds, took over. Surface erosion due to lateral and vertical displacements of meltwater and basal melt to the ocean flattened the floes (Figures 14c and 14d).

5. Summary and Perspectives

We reported continuous SIMBA observations in the high Arctic over the full 2013 summer season at two nearby sites A and B with distinct initial snow depths, ice thicknesses, and positions with respect to the local floe topography. Sea ice survived summer melt at the two sites which entered the refreezing season with similar snow and ice thicknesses. Although the two sites experienced similar atmospheric conditions, they showed contrasting evolution and processes as expected from the local ice topography (e.g., Eicken et al., 2004; Flocco & Fetham, 2007).

Site B with an initial thick sea ice (1.75 m) and thin snow layer (0.23 m) was at a high spot on its floe. Snow accumulated in May to reach a depth above 0.45 m. Later, meltwater either infiltrated sea ice or streamed away downslope and site B surface did not support any discernable accumulation of meltwater. Site B underwent a continuous basal loss from mid-June onward leading to 0.5-m basal ablation.

In contrast, Site A, with an initial thin sea ice (1.40 m) at a low location of the floe, witnessed the formation of a spectacular melt pond following a massive accumulation of snowmelt water. The pond reached a depth of 1.20 m over warm ice that was 1.10 m thick. The pond was well mixed, and its temperature showed a 0.5 °C diurnal cycle. The pond water eroded the ice surface leading to about 0.2-m surface ablation in 3 days. It outpoured into the ocean in about 6 hr. The fresh ice grew rapidly (0.65 m of fresh sea ice in 10 days; see Appendix A). Then turbulent conditions in the ocean associated with a large friction velocity (ice drift >0.2 m/s) resulted in an increase of the fluxes from the ocean to the ice and in turn a rapid ablation of the fresh ice (0.45 m in a week). At the end of summer, site A had almost recovered its initial ice thickness. The summer processes acted as leveling mechanisms of the sea ice (e.g., Notz et al., 2003; Perovich et al., 2003).

Apart from the surface erosion due to the melt pond, surface ice ablation was small, even there was surface accretion at site B with superposed ice that survived summer (+0.10 m). The small surface ice melt is related to the peculiar atmospheric conditions in summer 2013 (Wang et al., 2016). Indeed, air temperatures were low in summer 2013 compared to previous years (Lei et al., 2018) and did not favor strong ice melt. The Transpolar Drift Stream was weak (Lei et al., 2018), and the two sites deployed at the North Pole in April remained north of 84°N until September. Arctic atmospheric conditions in summer 2013 resulted in a 33% increase of sea ice volume in autumn 2013 compared with the 2010–2012 average (Tilling et al., 2015).

Perovich et al. (2014) examined ice losses due to summer surface and bottom melt over 9 years from 2000 to 2013 using data from ice mass balance buoys deployed at the North Pole and drifting toward Fram Strait. The data showed a large interannual variability in both surface (0.02 to 0.50 m) and bottom (0.10 to 0.57 m) melt and provided a surface ice melt of 0.22 m and a bottom ice melt of 0.38 m over summer 2013. Our results

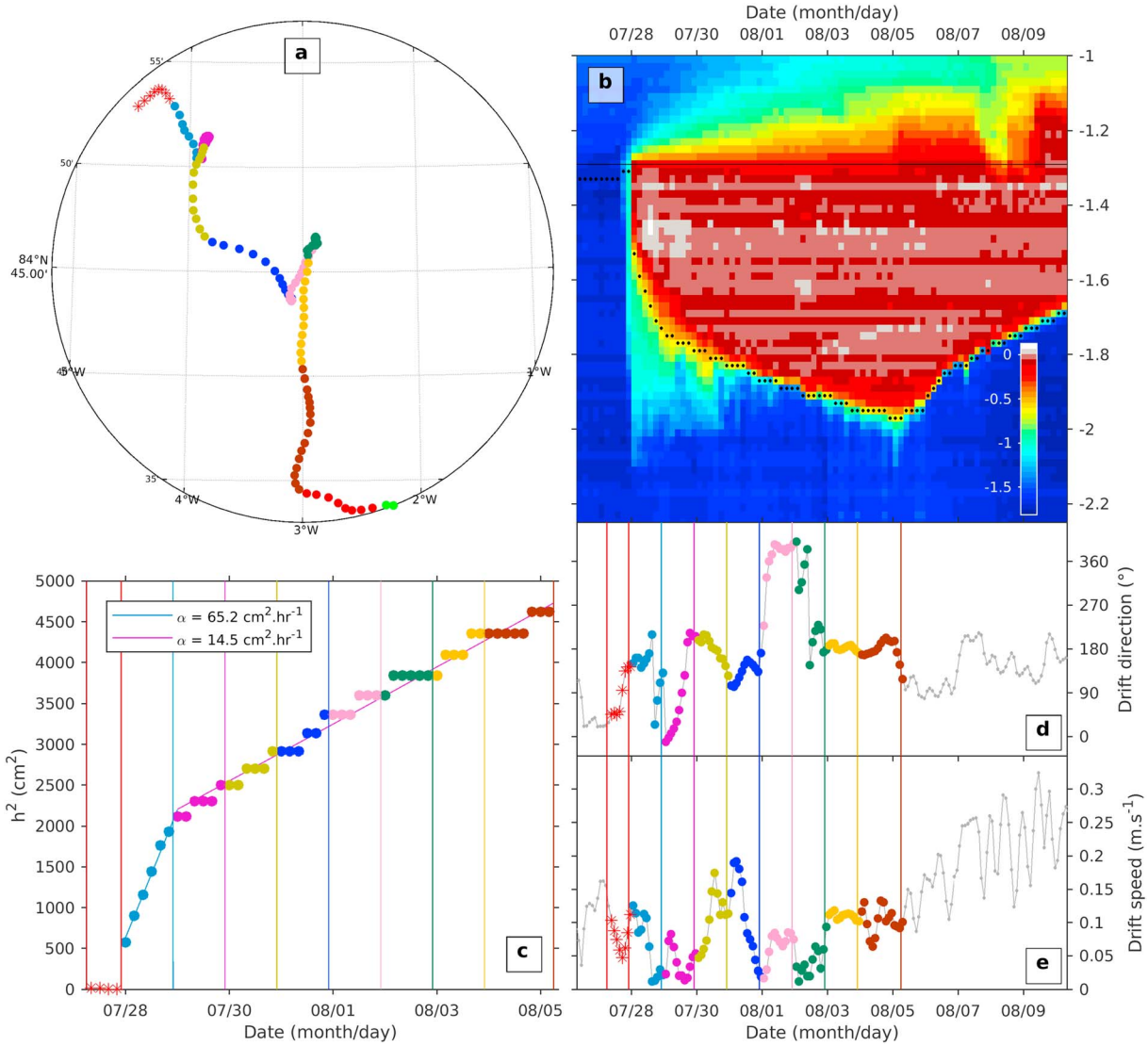

Figure A1. Close up on the false bottom ice growth. (a) Trajectory, with one dot every 2 hr, colors mark days. (b) Temperature (°C) from sea ice mass balance for the Arctic. *Y* axis is distance to the initial snow-ice interface. *X* axis is time with a tick every 2 days. (c) Square of the sea ice depth change h^2 (cm^2) as a function of time (different color every day). A straight line of slope α is fitted. There is a change in slope on 29 July. (d) Drift direction (degrees, north is 0, east is 90). (e) Drift speed (m/s).

with a surface ice change of −0.10 m at site A (+0.10 m at site B) and bottom ice change of 0 m at site A (−0.50 m at site B) point at a large spatial heterogeneity.

The SIMBA precisely documented several summer processes: the snowmelt, the formation and detachment of superimposed ice, the formation of a deep melt pond, the formation of interposed fresh ice plugs able to support the pond, the rapid freezing of the freshwater false bottom, and its subsequent dissolution. It is the first time that these processes have been continuously monitored. Our ongoing laboratory tank experiments show that the thin SIMBA chain (width 0.012 m, thickness 0.003 m) does not exert any major perturbation on the snow-ice system.

At the end of summer, site A ice was made of layers (Figure 12e), and in the absence of ice cores (none at deployment nor at recovery), the nature of these layers can only be hypothesized. Ice cores are highly desirable. Empirically, we were able to identify fresh ice plugs (with a ΔT_{120s} of 1.25 °C) using the SIMBA heating mode. The white layers are made of freshwater. We are investigating the SIMBA potential in further discriminating between snow types and ice types in laboratory tank experiments.

Appendix A: Close-Up of the False Bottom Growth

Site A pond drained in less than 6 hr on 28 July at a time of heavy rainfall associated with a stormy weather and a change in drift trajectory (Figure A1a). The ice formed from the fresh water mainly appeared just under the sea ice and thickened rapidly (0.65 cm of fresh ice was produced in 10 days; see section 3.2.3).

A false bottom usually is defined as a layer of ice that imprisons a layer of fresh water under old ice (Martin & Kauffman, 1974; Notz et al., 2003). Here, observations strongly suggest that such a false bottom cannot be maintained for long, perhaps because of the ocean turbulence and of the large dimensions of the under-ice pond. The ice crystals that formed were less dense than fresh water and migrated upward, up to the old ice. Consequently, the ice formed from fresh water mainly appeared just under the old sea ice. Note however that hints of false bottoms can be seen from the temperature profile (Figure 8d). The old sea ice was colder than the layer of newly formed fresh ice (Figure 8). There was, therefore, a heat flux that slightly cooled down the newly formed ice and warmed up the old sea ice.

Simple analytic models provide rather good results for sea ice growth (Leppäranta, 1993). Notz et al. (2003) proposed a simple model of false bottom formation in which the ice thickness $h(t)$ varies following the law:

$$h^2(t) = 4\,(\lambda_u - \lambda)^2\,D\,t$$

where D is a salinity diffusion coefficient and λ_u and λ are two constants (order of magnitude 1.5) characterizing growth λ_u and ablation λ (cf. equations (12), (13), and (14) in Notz et al., 2003).

During the first days the constant of proportionality $4\,(\lambda_u - \lambda)^2\,D$ was about 65 cm^2/hr providing an estimate for D of 4.5×10^{-7} m^2/s with $(\lambda_u - \lambda)$ on the order of one (weak ablation, e.g., $\lambda_u \sim 1.5$ and $\lambda \sim 0.5$; Figure A1c). This turbulent diffusion coefficient is 1,000 times larger than the estimates in quiescent conditions 7.5×10^{-10} m^2/s reported by Martin and Kauffman (1974). Then the regime changed, and, during the following 7 days, the same law was verified with a constant of proportionality $4\,(\lambda_u - \lambda)^2\,D$ reduced to 14.5 cm^2/hr (Figure A1c). The change in growth rate does not bear any clear relation to changes in drift direction or drift velocity (Figure A1d). Thus, the turbulent conditions being similar, D probably does not change much. Thus, $(\lambda_u - \lambda)$ is divided by 2, suggesting an increased ablation (e.g., $\lambda_u \sim 1.5$ and $\lambda \sim 1$) reducing the ice growth. We speculate that as the layer of fresh water became thinner, the impact of the underlying seawater became stronger and dissolution competed with ice formation. This interpretation is consistent with Notz et al. (2003; their Figure 6; a salinity change of about +2.5 psu induces an increase of 0.5 in λ).

Acknowledgments

We are indebted to Jean-Claude Gascard (LOCEAN, France), Jamie Morison and his team from APL (University of Washington, USA), and Sergey Pisarev (Shirshov Institute, Russia) who contributed to deployments of the instruments from the Barneo ice camp at the North Pole in 2013. We also thank the team onboard Norwegian ice breaker KV Svalbard and the scientific leader of the under-ice cruise (Hanne Sagen, Nansen Center, Norway) for permitting the recovery of the instruments. Michael Field is thanked for his help during the cruise. Michael Field and Clément Weber participated to the careful examination of the webcam images. Aude Dupin contributed to Figure 14. We are thankful to two anonymous reviewers for their constructive comments and to Editor Laurie Padman for his thorough editing. We acknowledge support from the ANR EQUIPEX IAOOS project, through ANR-10-EQPX-32-01 grant. Parameters from the ERA-Interim reanalysis were obtained from ECMWF. The webcam images were produced at APL and are available online (ftp://northpoleftp.apl.washington.edu/NPEO_WebCam_Image_Archive/NPEO_2013_WebCam#2/). The SIMBA data are publicly available in the SEANOE database (https://doi.org/10.17882/58796; Sennéchael et al., 2019).

References

Athanase, M., Sennéchael, N., Garric, G., Koenig, Z., Boles, E., & Provost, C. (2019). New hydrographic measurements of the upper Arctic western Eurasian Basin in 2017 reveal fresher mixed layer and shallower warm layer than 2005-2012 climatology. *Journal of Geophysical Research: Oceans*, *124*, 1091–1114. https://doi.org/10.1029/2018JC014701

Dee, D. P., Uppala, S. M., Simmons, A. J., Berrisford, P., Poli, P., Kobayashi, S., et al. (2011). The ERA-Interim reanalysis: Configuration and performance of the data assimilation system. *Quarterly Journal of the Royal Meteorological Society*, *137*(656), 553–597. https://doi.org/10.1002/qj.828

Eicken, H. (1994). Structure of under ice melt ponds in the Central Arctic and their effect on sea-ice cover. *Limnology and Oceanography*, *39*(3), 682–693. https://doi.org/10.4319/lo.1994.39.3.0682

Eicken, H., Grenfell, T. C., Perovich, D. K., Richter-Menge, J. A., & Frey, K. (2004). Hydraulic controls of summer Arctic pack ice albedo. *Journal of Geophysical Research*, *109*, C08007. https://doi.org/10.1029/2003JC001989

Eicken, H., Krouse, H. R., Kadko, D., & Perovich, D. K. (2002). Tracer studies of pathways and rates of meltwater transport through Arctic summer sea ice. *Journal of Geophysical Research*, *107*(C10), 8046. https://doi.org/10.1029/2000JC000583

Feltham, D. L., Untersteiner, N., Wettlaufer, J. S., & Worster, M. G. (2006). Sea ice is a mushy layer. *Geophysical Research Letters*, *33*, L14501. https://doi.org/10.1029/2006GL026290

Flocco, D., & Fetham, D. L. (2007). A continuum model of melt pond evolution on Arctic sea ice. *Journal of Geophysical Research*, *112*, C08016. https://doi.org/10.1029/2006JC003836

Golden, K. M., Eicken, H., Heaton, A. L., Miner, J., Pringle, D. J., & Zhu, J. (2007). Thermal evolution of permeability and microstructure in sea ice. *Geophysical Research Letters*, *34*, L16501. https://doi.org/10.1029/2007/GL030447

Jackson, K., Wilkinson, J., Maksym, T., Meldrum, D., Beckers, J., Haas, C., & Mackenzie, D. (2013). A novel and low-cost sea ice mass balance buoy. *Journal of Atmospheric and Oceanic Technology*, *30*(11), 2676–2688. https://doi.org/10.1175/JTECH-D-13-00058

Lei, R., Cheng, B., Heil, P., Vihma, T., Wang, J., Ji, Q., & Zhang, Z. (2018). Seasonal and interannual variations of sea ice mass balance from the Central Arctic to Greenland Sea. *Journal of Geophysical Research: Oceans*, *123*, 2422–2439. https://doi.org/10.1002/2017JC013548

Leppäranta, M. (1993). A review of analytical models of sea-ice growth. *Atmosphere-Ocean*, *31*(1), 123–138. https://doi.org/10.1080/07055900.1993.9649465

Martin, S., & Kauffman, P. (1974). The evolution of under-ice meltponds, or double diffusion at the freezing point. *Journal of Fluid Mechanics*, *64*(3), 507–528. https://doi.org/10.1017/S0022112074002527

Notz, D., Mc Phee, M. G., Worster, M. G., Maykut, G. A., Schlunzen, K. H., & Eicken, H. (2003). Impact of underwater-ice evolution on Arctic summer sea-ice. *Journal of Geophysical Research*, *108*(C7), 3223. https://doi.org/10.1029/2001JC001173

Notz, D., & Worster, M. G. (2009). Desalination processes of sea ice revisited. *Journal of Geophysical Research*, *114*, C05006. https://doi.org/10.1029/2008JC004885

Perovich, D. K., Greenfell, T. C., Richter-Menge, A., Light, B., Tucker, W. B. III, & Eicken, H. (2003). Thin and thinner: Sea ice mass balance measurements during SHEBA. *Journal of Geophysical Research*, *108*(C3), 8050. https://doi.org/10.1029/2001JC001079

Perovich, D. K., Grenfell, T. C., Light, B., & Hobbs, P. V. (2002). Seasonal evolution of the albedo of multiyear Arctic sea ice. *Journal of Geophysical Research*, *107*(C10), 8044. https://doi.org/10.1029/2000JC000438

Perovich, D. K., Richter-Menge, J., Polashenski, C., Elder, B., Arbetter, T., & Brennick, O. (2014). Sea ice mass balance observations from the North Pole Environmental Observatory. *Geophysical Research Letters*, *41*, 2019–2025. https://doi.org/10.1002/2014GL059356

Polashenski, C., Golden, K. M., Perovich, D. K., Skyllingstad, E., Arnsten, A., Stwertka, C., & Wright, N. (2017). Percolation blockage: A process that enables melt pond formation on first year Arctic sea ice. *Journal of Geophysical Research: Oceans*, *122*, 413–440. https://doi.org/10.1002/2016JC011994

Polashenski, C., Perovich, D., & Courville, Z. (2012). The mechanisms of sea ice melt pond formation and evolution. *Journal of Geophysical Research*, *117*, C01001. https://doi.org/10.1029/2011JC007231

Provost, C., Sennéchael, N., Miguet, J., Itkin, P., Rosel, A., Koenig, Z., et al. (2017). Observations of flooding and snow-ice formation in a thinner Arctic sea-ice regime during the N-ICE2015 campaign: Influence of basal ice melt and storms. *Journal of Geophysical Research: Oceans*, *122*, 7115–7134. https://doi.org/10.1002/2016JC012011

Sennéchael, N., Provost, C., Gascard, J.-C., Calzas, M., Drezen, C., Garracio, M. (2019). SIMBA data acquired during IAOOS drifts from the North-Pole to Fram Strait in 2013. SEANOE. https://doi.org/10.17882/58796

Simmons, A. J., & Poli, P. (2015). Arctic warming in ERA-Interim and other analyses. *Quarterly Journal of the Royal Meteorological Society*, *141*(689), 1147–1162. https://doi.org/10.1002/qj.2422

Tilling, R. L., Ridout, A., Shepherd, A., & Wingham, D. J. (2015). Increased Arctic sea ice volume after anomalously low melting in 2013. *Nature Geoscience*, *8*(8), 643–646, ISSN 1752-0894. https://doi.org/10.1038/NGEO2489

Wang, C., Granskog, M. A., Hudson, S. R., Gerland, S., Pavlov, A. K., Perovich, D. K., & Nicolaus, M. (2016). Atmospheric conditions in the central Arctic Ocean through the melt seasons of 2012 and 2013: Impact on surface conditions and solar energy deposition into the ice-ocean system. *Journal of Geophysical Research: Atmospheres*, *121*, 1043–1058. https://doi.org/10.1002/2015JD023712

Woods, A. W. (1992). Melting and dissolving. *Journal of Fluid Mechanics*, *239*(1), 429–448. https://doi.org/10.1017/S0022112092004476